

A Finite Difference Method for Off-fault Plasticity throughout the Earthquake Cycle

Brittany A. Erickson^a, Eric M. Dunham^{b,c}, Arash Khosravifar^d

^a*Department of Mathematics and Statistics, Portland State University, Portland, OR 97201, USA. berickson@pdx.edu*

^b*Department of Geophysics, Stanford University, Stanford, CA, USA.*

^c*Institute for Computational & Mathematical Engineering, Stanford University, Stanford, CA, USA.*

^d*Department of Civil and Environmental Engineering, Portland State University, Portland, OR, USA.*

Abstract

We have developed an efficient computational framework for simulating multiple earthquake cycles with off-fault plasticity. The method is developed for the classical antiplane problem of a vertical strike-slip fault governed by rate-and-state friction, with inertial effects captured through the radiation-damping approximation. Both rate-independent plasticity and viscoplasticity are considered, where stresses are constrained by a Drucker-Prager yield condition. The off-fault volume is discretized using finite differences and tectonic loading is imposed by displacing the remote side boundaries at a constant rate. Time-stepping combines an adaptive Runge-Kutta method with an incremental solution process which makes use of an elastoplastic tangent stiffness tensor and the return-mapping algorithm. Solutions are verified by convergence tests and comparison to a finite element solution. We quantify how viscosity, isotropic hardening, and cohesion affect the magnitude and off-fault extent of plastic strain that develops over many ruptures. If hardening is included, plastic strain saturates after the first event and the response during subsequent ruptures is effectively elastic. For viscoplasticity without hardening, however, successive ruptures continue to generate additional plastic strain. In all cases, coseismic slip in the shallow sub-surface is diminished compared to slip accumulated at depth during interseismic loading. The evolution of this slip deficit with each subsequent event, however, is dictated by the plasticity model. Integration of the off-fault plastic strain from the viscoplastic model reveals that a significant amount of tectonic off-

set is accommodated by inelastic deformation (~ 0.1 m per rupture, or $\sim 10\%$ of the tectonic deformation budget).

Keywords: earthquake cycle, plasticity, Drucker-Prager, finite difference method

1 Introduction

Field observations reveal regions of highly damaged rock (containing abundant microfractures) surrounding a fault core, which many attribute to thousands of years of seismogenic cycling during which earthquakes shatter the rocks in the vicinity of the fault (*Chester and Logan, 1986; Chester et al., 1993; Shipton et al., 2005; Mitchell and Faulkner, 2009; Faulkner et al., 2010; Ben-Zion and Sammis, 2011*). Understanding how an earthquake will propagate is intimately tied to the evolution of these damage zones. Important and unsolved problems include the relationship between the degree of off-fault yielding and mechanical properties of fault zone material, how damage zones evolve with increasing cumulative slip, and how damage zones affect subsequent rupture.

Current models for dynamic rupture have led to much insight into earthquake propagation, the generation of high-frequency ground motion, and the influence of plasticity on rupture propagation (*Templeton and Rice, 2008; Ma and Andrews, 2010; Dunham et al., 2011a,b; Kaneko and Fialko, 2011; Xu et al., 2012a,b; Shi and Day, 2013; Gabriel et al., 2012, 2013*). Although the inclusion of a plastic material response has been shown to reduce stress and slip velocities at the rupture front to reasonable values, little work has been done to understand the evolution of a damage zone (and its impact on rupture) over multiple event sequences. In particular, most dynamic rupture models currently make the assumption of a uniform background stress and are limited to single-event simulations where rupture is artificially initiated via a stress perturbation imposed on the fault. Earthquake cycle models, on the other hand, generate self-consistent initial conditions because of their ability to handle varying time scales. Cycle models developed in the boundary integral or boundary element context were limited to simulations in a uniform, linear elastic whole- or half-space (*Lapusta et al., 2000; Tullis et al., 2012*). Recent developments, however, have shown how to incorporate more realistic features (material heterogeneities or inelastic deformation, for example) into the earthquake cycle framework (*Johnson and Segall, 2004; Kaneko*

32 *et al.*, 2011; *Barbot et al.*, 2012; *Aagaard et al.*, 2013; *Erickson and Dunham*,
33 2014; *Thompson and Meade*, 2016; *Allison and Dunham*, 2017).

34 In this work we study the role of plasticity throughout the earthquake
35 cycle. The computational method is developed for the classical antiplane
36 problem of a vertical strike-slip fault governed by rate-and-state friction.
37 The off-fault material is idealized as a Drucker-Prager elastic-plastic solid
38 and stresses are constrained by a depth-dependent yield condition. Inertia
39 is approximated with radiation damping. Within the context of a time-
40 stepping method, we solve the resulting equilibrium equation (a nonlinear,
41 elliptic partial differential equation) for the displacement increment.

42 Although computational plasticity is most commonly addressed in a finite
43 element framework, we develop a finite difference method, as the latter is
44 easy to program, efficient, and can be applied in a straightforward manner in
45 order to obtain a numerical approximation to the solution (*Scalerandi et al.*,
46 1999). Recent work in summation-by-parts finite difference methods has
47 furnished high-order accurate schemes that enforce boundary and interface
48 conditions in a stable manner (through the simultaneous-approximation-term
49 technique) (*Kreiss and Scherer*, 1974, 1977; *Nordström et al.*, 2007; *Svärd*
50 *and Nordström*, 2014). These methods provide a framework for proving
51 convergence for linear and nonlinear problems, which is fundamental in order
52 to obtain credible numerical approximations. In this work, an initial analysis
53 is done of the underlying continuum problem to show it satisfies an energy
54 estimate (in this case, dissipation of mechanical energy in the absence of non-
55 trivial boundary conditions or source terms). The computational method
56 then provides a spatial discretization that mimics the energy estimate of the
57 continuum problem and proves stability of the method.

58 The paper is organized as follows: In section 2 we state the continuum
59 problem solved in this work. A rate-and-state frictional fault is embedded in
60 an elastoplastic solid and the equation for static equilibrium is solved within
61 the context of a time-stepping method that imposes remote loading and fault
62 slip (in a manner consistent with a fault friction law), deferring specific de-
63 tails to later sections. Section 3 provides details of the Drucker-Prager model
64 for rate-independent plasticity that defines the constitutive relation (as vis-
65 coplasticity is a straight-forward extension of the associated algorithms, de-
66 tailed in section 7.2). This is described in terms of the material response at
67 a particular point in the solid, and provides a procedure for evolving stress
68 and plastic strain given a history of total strain. Section 4 applies the results
69 of section 3, detailing the derivation of the incremental form of the contin-

70 uum problem of section 2 and obtaining the governing equation solved within
 71 the time-stepping method. In section 5 we show conditions under which the
 72 resulting boundary value problem for the solid satisfies the Drucker stabil-
 73 ity condition. We also establish conservation of the incremental internal
 74 energy in the absence of nontrivial boundary conditions. Section 6 details
 75 the spatial discretization, specifically a finite difference method for variable
 76 coefficients satisfying a summation-by-parts (SBP) rule with weak enforce-
 77 ment of boundary conditions through the simultaneous-approximation-term
 78 (SAT) technique. The combined method will be denoted throughout the
 79 paper as SBP-SAT. We show that the semi-discrete problem using the SBP-
 80 SAT method mimics the energy balance of the continuum problem. In sec-
 81 tion 7 we describe the time stepping method for the overall problem. The
 82 solid displacement, stress, and plastic strain are updated in response to time-
 83 dependent boundary conditions obtained by updating fault slip in a manner
 84 consistent with the friction law. At each time step we solve numerically
 85 the incremental equilibrium equation for the solid using an iterative Newton
 86 procedure with the return mapping algorithm to calculate stresses consistent
 87 with the constitutive theory. The extension of the algorithms to viscoplas-
 88 ticity is also detailed. In section 8 we present convergence tests and compar-
 89 isons with numerical solutions from a finite element code to verify our finite
 90 difference method. In section 9 we apply our method to earthquake cycle
 91 simulations, and conclude in section 10 with a discussion.

92 2. The Continuum Problem

93 In this work we assume two-dimensional antiplane shear deformation. The
 94 equation for static equilibrium in the medium is given by

$$95 \quad \frac{\partial \sigma_{xy}}{\partial y} + \frac{\partial \sigma_{xz}}{\partial z} = 0, \quad (y, z) \in [-L_y, L_y] \times [0, L_z], \quad (1)$$

96 where σ_{xy} and σ_{xz} are the relevant components of the stress tensor σ . The
 97 constitutive relation (Hooke's law) relates stress to elastic strain through the
 98 relations

$$99 \quad \sigma_{xy} = \mu(\gamma_{xy} - \gamma_{xy}^p), \quad (2a)$$

$$100 \quad \sigma_{xz} = \mu(\gamma_{xz} - \gamma_{xz}^p), \quad (2b)$$

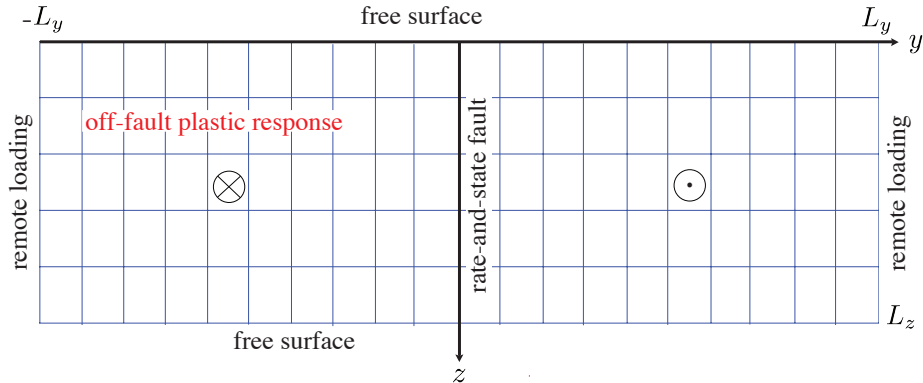


Figure 1: Schematic diagram for antiplane shear deformation where $u(t, y, z)$ is the out-of-plane displacement. We displace the sides $y = \pm L_y$ at a constant rate, with free surface conditions on the top and bottom. A frictional fault at $y = 0$ is embedded in an elastic-plastic medium.

101 for out-of-plane displacement $u(t, y, z)$, shear modulus μ , total engineering
 102 strains

$$103 \quad \gamma_{xy} = \partial u / \partial y \quad (3a)$$

$$104 \quad \gamma_{xz} = \partial u / \partial z, \quad (3b)$$

105 and plastic engineering strains $\gamma_{xy}^p, \gamma_{xz}^p$. Plastic deformation evolves according
 106 to a flow rule of the form

$$107 \quad \dot{\gamma}_{xy}^p = \lambda P_{xy}, \quad (4a)$$

$$108 \quad \dot{\gamma}_{xz}^p = \lambda P_{xz}, \quad (4b)$$

109 where λ is the magnitude of the plastic strain rate (a positive, scalar function
 110 of the stress), which is nonzero only when plastic deformation occurs. P_{xy}, P_{xz}
 111 are dimensionless, (generally nonlinear) functions of the stress, determine
 112 how the plastic strain rate is partitioned between different components, and
 113 specified by the particular plasticity model (*Chen and Han, 1988; Simo and*
 114 *Hughes, 1998*). More details are given in section 3.

115 A vertical, strike slip fault governed by a rate-and-state friction law lies
 116 at the interface $y = 0$ (*Dieterich, 1979; Ruina, 1983*) (see Figure 1) where
 117 we impose the condition that the jump in displacement is equal to the fault
 118 slip, Δu , namely

$$119 \quad u(t, 0^+, z) - u(t, 0^-, z) = \Delta u(t, z). \quad (5)$$

120 In addition, we require that the components of the traction vector on the
 121 fault be equal and opposite across the interface, which, for antiplane motion,
 122 reduces to the second interface condition

$$123 \quad \sigma_{xy}(t, 0^+, z) = \sigma_{xy}(t, 0^-, z). \quad (6)$$

124 Slow tectonic loading is imposed by displacing the remote boundaries at a
 125 constant relative rate V_p and the top and bottom boundaries are assumed
 126 to be free surfaces. We assume the solution u is anti-symmetric across the
 127 fault interface (i.e. $u(t, y, z) = -u(t, -y, z)$ for $0 \leq y \leq L_y$) so that (6)
 128 is satisfied by construction, and so we may focus on one side of the fault,
 129 namely $(y, z) \in [0, L_y] \times [0, L_z]$ (see *Erickson and Dunham (2014)* for details
 130 and a discussion on the choice of boundary conditions). For the one-sided
 131 problem the boundary conditions are thus given by

$$132 \quad u(t, 0, z) = \Delta u/2, \quad (7a)$$

$$133 \quad u(t, L_y, z) = V_p t/2, \quad (7b)$$

$$134 \quad \sigma_{xz}(t, y, 0) = 0, \quad (7c)$$

$$135 \quad \sigma_{xz}(t, y, L_z) = 0. \quad (7d)$$

136 In the rate-and-state friction framework, shear stress on the fault, denoted
 137 τ (and related to σ_{xy} as detailed below), is equated with frictional strength
 138 through the relation

$$139 \quad \tau = \sigma_n f(V, \psi), \quad (8)$$

140 where

$$141 \quad V = \Delta \dot{u} \quad (9)$$

142 denotes the slip velocity, ψ is an internal state variable, σ_n is the effective
 143 normal stress and f is a friction coefficient that takes the particular form

$$144 \quad f(V, \psi) = a \sinh^{-1} \left(\frac{V}{2V_0} e^{\psi/a} \right) \quad (10)$$

145 (*Dieterich, 1979; Ruina, 1983*). We assume the state variable ψ evolves to
 146 the aging law form of evolution, namely

$$147 \quad \frac{d\psi}{dt} = \frac{bV_0}{D_c} \left(e^{(f_0 - \psi)/b} - \frac{V}{V_0} \right). \quad (11)$$

148 With the aging law, state can evolve in the absence of slip, and therefore
 149 may be more suitable for modeling the interseismic period. In equations (10)
 150 and (11), a and b are dimensionless parameters quantifying the direct effect
 151 and state evolution, respectively, f_0 is a reference friction at a reference slip
 152 velocity V_0 , and D_c is the state evolution distance (*Marone, 1998*).

153 In section 7 we describe how the slip Δu is obtained in a manner consistent
 154 with the fault friction law (8), where τ is related to σ_{xy} through the following.
 155 Solving the equilibrium equation (1) provides the quasistatic stresses σ_{xy}, σ_{xz} .
 156 Since disregarding inertia entirely is known to cause slip velocity $V \rightarrow \infty$
 157 in finite time (after which no solution exists), we incorporate the radiation
 158 damping approximation to inertia (*Rice, 1993*). Thus τ is defined to be

$$159 \quad \tau = \sigma_{xy}(t, 0, z) - \eta_{rad}V \quad (12)$$

160 where $-\eta_{rad}V$ is the stress due to radiation damping and $\eta_{rad} = \mu/(2c_s)$
 161 is half the shear-wave impedance (not to be confused with viscosity η for
 162 viscoplastic flow) for shear wave speed $c_s = \sqrt{\mu/\rho}$ and material density ρ .

163 3. Elastoplastic Constitutive Theory

164 In this section we review the Drucker-Prager elastoplastic constitutive
 165 theory that is used to evolve stress and plastic strain (in response to an
 166 imposed total strain history at a particular material point).

167 3.1. Drucker-Prager Plasticity

168 Throughout this work we assume infinitesimal strains. Hooke's law (intro-
 169 duced in (2) for the antiplane setting) can be expressed generally by

$$170 \quad \sigma = C : (\epsilon - \epsilon^p) \quad (13)$$

171 where ϵ and ϵ^p are the total and plastic strain tensors. The fourth order
 172 elasticity tensor C_{ijkl} for an isotropic solid is given by

$$173 \quad C_{ijkl} = K\delta_{ij}\delta_{kl} + \mu(\delta_{ik}\delta_{jl} + \delta_{il}\delta_{jk} - (2/3)\delta_{ij}\delta_{kl}), \quad (14)$$

174 where K is the bulk modulus. Stresses in the medium are constrained by a
 175 Drucker-Prager yield condition, see Figure 2. For rate-independent response
 176 with linear, isotropic hardening, the yield function is given by

$$177 \quad F(\sigma, \gamma^p) = \bar{\tau} - (\sigma_Y + h\gamma^p), \quad (15)$$

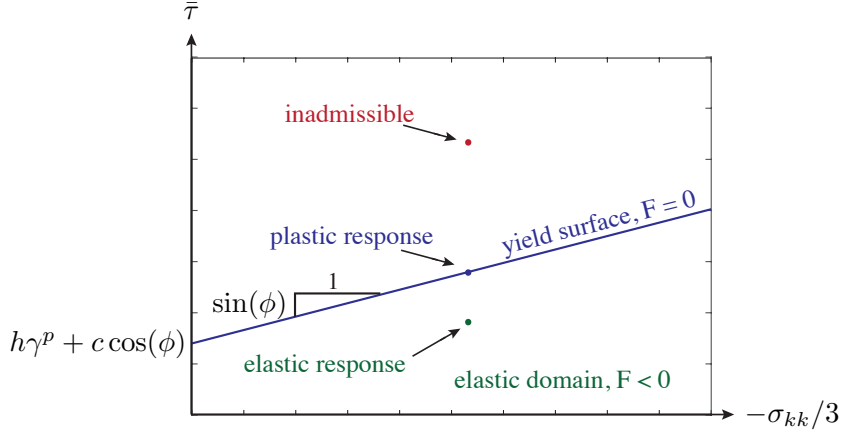


Figure 2: The Drucker-Prager yield condition for yield function F . Elastic response occurs for states of stress that lie below the yield surface, while plastic response occurs for states on the surface. States above the yield surface are inadmissible. The slope of the line is defined by the angle of internal friction ϕ , while the y -intercept depends further on cohesion c and hardening modulus h .

178 where γ^p is the hardening parameter (equivalent plastic strain, defined below)
 179 and h is the hardening modulus. In this work we assume $h > 0$ is constant (we
 180 say the response is strain-softening if $h < 0$, and perfectly plastic if $h = 0$).
 181 The elastic domain in stress space is given by $\mathbb{E}_\sigma = \{(\sigma, \gamma^p) : F(\sigma, \gamma^p) \leq 0\}$
 182 and plastic flow ensues when the yield condition

$$183 \quad F(\sigma, \gamma^p) = 0 \quad (16)$$

184 is met. The second invariant of the deviatoric stress is

$$185 \quad \bar{\tau} = \sqrt{s_{ij}s_{ij}/2} \quad (17)$$

186 for $s_{ij} = \sigma_{ij} - \sigma_{kk}\delta_{ij}/3$. The yield stress is given by

$$187 \quad \sigma_Y = -(\sigma_{kk}/3) \sin \phi + c \cos \phi, \quad (18)$$

188 where c is the cohesion and ϕ is the internal friction angle. Plastic strain
 189 evolves according to the flow rule (introduced in equation (4)) given by

$$190 \quad \dot{\epsilon}_{ij}^p = \lambda P_{ij}, \quad (19)$$

191 where $\lambda = \sqrt{2\dot{e}_{ij}^p \dot{e}_{ij}^p}$ is the deviatoric plastic strain rate for $e_{ij}^p = \epsilon_{ij}^p - \epsilon_{kk}^p \delta_{ij}/3$.

192 Thus

$$193 \quad \gamma^p(t) = \int_0^t \lambda(s) ds, \quad (20)$$

194 and P_{ij} (specified in the next section) quantifies how plastic strain is dis-
 195 tributed between different components of the plastic strain rates. The con-
 196 stitutive theory is closed by including the Kuhn-Tucker loading/unloading
 197 (complementarity) conditions

$$198 \quad \lambda \geq 0, \quad F \leq 0, \quad \lambda F = 0, \quad (21)$$

199 (which ensure that plastic flow can only occur if stresses lie on the yield
 200 surface) and the consistency (persistence) condition

$$201 \quad \lambda \dot{F} = 0, \quad (22)$$

202 so that if plastic flow occurs, the stress state must persist on the yield surface
 203 for some positive period of time.

204 3.2. Elastoplastic Tangent Stiffness Tensor

205 In rate form, Hooke's law (13) expresses stress rate in terms of total strain
 206 rate, namely

$$207 \quad \dot{\sigma}_{ij} = C_{ijkl}^{ep} \dot{\epsilon}_{kl}, \quad (23)$$

208 where the continuum elastoplastic tangent stiffness tensor $C_{ijkl}^{ep} = C_{ijkl}^{ep}(\sigma)$
 209 is a nonlinear function of stress. We derive this tensor following *Simó and*
 210 *Hughes* (1998), by first taking the time derivative of the yield function, and
 211 then using (19) and the time derivative of (20):

$$212 \quad \begin{aligned} \dot{F} &= \frac{\partial F}{\partial \sigma_{ij}} \dot{\sigma}_{ij} + \frac{\partial F}{\partial \gamma^p} \dot{\gamma}^p = \frac{\partial F}{\partial \sigma_{ij}} C_{ijkl} (\dot{\epsilon}_{kl} - \dot{\epsilon}_{kl}^p) + \frac{\partial F}{\partial \gamma^p} \dot{\gamma}^p \\ 213 \quad &= \frac{\partial F}{\partial \sigma_{ij}} C_{ijkl} \dot{\epsilon}_{kl} - \lambda \left(\frac{\partial F}{\partial \sigma_{ij}} C_{ijkl} P_{kl} - \frac{\partial F}{\partial \gamma^p} \right). \end{aligned} \quad (24)$$

214 Assuming that

$$215 \quad \left(\frac{\partial F}{\partial \sigma_{ij}} C_{ijkl} P_{kl} - \frac{\partial F}{\partial \gamma^p} \right) > 0, \quad (25)$$

216 (in order to ensure consistency with (21)-(22), see *Simo and Hughes* (1998)
 217 for more details), we can solve $\dot{F} = 0$ for λ , namely

$$218 \quad \lambda = \frac{\langle \frac{\partial F}{\partial \sigma_{ij}} C_{ijkl} \dot{\epsilon}_{kl} \rangle}{\frac{\partial F}{\partial \sigma_{mn}} C_{mnop} P_{op} - \frac{\partial F}{\partial \gamma^p}}, \quad (26)$$

219 where the brackets denote the ramp function $\langle x \rangle = \frac{x+|x|}{2}$. Taking the time
 220 derivative of the stress and substituting in the flow rule yields

$$221 \quad \dot{\sigma}_{ij} = C_{ijkl} (\dot{\epsilon}_{kl} - \lambda P_{kl}) = C_{ijkl} \left(\dot{\epsilon}_{kl} - \frac{\langle \frac{\partial F}{\partial \sigma_{mn}} C_{mnop} \dot{\epsilon}_{op} \rangle}{\frac{\partial F}{\partial \sigma_{qr}} C_{qrst} P_{st} - \frac{\partial F}{\partial \gamma^p}} P_{kl} \right), \quad (27)$$

222 which allows us to express the continuum elastoplastic tangent stiffness tensor

$$223 \quad C_{ijkl}^{ep} = \begin{cases} C_{ijkl} & \text{if } \lambda = 0, \\ C_{ijkl} - \frac{C_{ijop} P_{op} C_{mnkl} \frac{\partial F}{\partial \sigma_{mn}}}{\frac{\partial F}{\partial \sigma_{qr}} C_{qrst} P_{st} - \frac{\partial F}{\partial \gamma^p}} & \text{if } \lambda > 0. \end{cases} \quad (28)$$

224 Note that C^{ep} is symmetric in the same manner as the elastic tensor given
 225 in (14) (namely, that $C_{ijkl}^{ep} = C_{jikl}^{ep} = C_{ijlk}^{ep} = C_{klij}^{ep}$), if the flow rule (19) is
 226 associative (i.e. if $P_{ij} = \frac{\partial F}{\partial \sigma_{ij}}$). For Drucker-Prager plasticity,

$$227 \quad P_{ij} = s_{ij}/(2\bar{\tau}) + (\beta/3)\delta_{ij}, \quad (29)$$

228 where β determines the degree of plastic dilatancy. Thus the flow rule is
 229 associative only if $\beta = \sin(\phi)$.

230 Expression (28) is thus

$$231 \quad C_{ijkl}^{ep} = \begin{cases} C_{ijkl} & \text{if } \lambda = 0, \\ C_{ijkl} - \frac{\frac{\mu^2}{\bar{\tau}^2} s_{ij} s_{kl} + \frac{\mu K}{\bar{\tau}} [\sin(\phi) s_{ij} \delta_{kl} + \beta \delta_{ij} s_{kl}] + \beta K^2 \sin(\phi) \delta_{ij} \delta_{kl}}{\mu + \beta K \sin(\phi) + h} & \text{if } \lambda > 0 \end{cases} \quad (30)$$

232 and associativity (symmetry of C_{ijkl}^{ep}) holds in the general case if $\beta = \sin \phi$.

233 4. The Governing Equation in Incremental Form

234 Because of the nonlinearity of the constitutive relation (2), a typical ap-
 235 proach taken is to consider the rate form, given by (23), and posit the equi-
 236 librium equation (1) in terms of an infinitesimal displacement increment du

237 (*Chen and Han, 1988; Simo and Hughes, 1998; Dunne and Petrinic, 2006*).
 238 In this section we derive the incremental equilibrium equation as well as the
 239 specific forms of the relevant elastoplastic moduli. Note that although du
 240 is an infinitesimally small increment in the continuum setting, it is taken to be
 241 finite when the problem is discretized in time as done in section 7.

242 In the case of antiplane strain, the only non-zero strains are γ_{xy}, γ_{xz} .
 243 For notational purposes, we therefore denote the relevant components of
 244 the fourth-order tensor C as $C_{xyxy} = C_{11}, C_{xyxz} = C_{12}, C_{xzyx} = C_{21}$, and
 245 $C_{xzxz} = C_{22}$. We use similar notation to denote relevant components of the
 246 elastoplastic tangent stiffness tensor, C^{ep} , introduced in the previous section.
 247 Using the rate form (23) allows us to replace (2) with an expression solely in
 248 terms of increments of stress $d\sigma$ and strain $d\gamma$, namely

$$249 \quad d\sigma_{xy} = C_{11}^{ep} d\gamma_{xy} + C_{12}^{ep} d\gamma_{xz}, \quad (31a)$$

$$250 \quad d\sigma_{xz} = C_{21}^{ep} d\gamma_{xy} + C_{22}^{ep} d\gamma_{xz}, \quad (31b)$$

251 where

$$252 \quad d\gamma_{xy} = \frac{\partial du}{\partial y}, \quad d\gamma_{xz} = \frac{\partial du}{\partial z} \quad (32)$$

253 are the incremental total engineering strains and du is the (infinitesimal)
 254 displacement increment. Relations (31), along with the strain-displacement
 255 relations (32) are substituted into the incremental form of the equilibrium
 256 equation (1) and produce the nonlinear equilibrium equation for du given by

$$257 \quad \frac{\partial}{\partial y} \left[C_{11}^{ep} \frac{\partial du}{\partial y} + C_{12}^{ep} \frac{\partial du}{\partial z} \right] + \frac{\partial}{\partial z} \left[C_{21}^{ep} \frac{\partial du}{\partial y} + C_{22}^{ep} \frac{\partial du}{\partial z} \right] = 0. \quad (33)$$

258 Recall that the elastoplastic moduli $C_{11}^{ep}, C_{12}^{ep}, C_{21}^{ep}$ and C_{22}^{ep} in equation (33)
 259 depend nonlinearly on the stress. Forming the 2×2 matrix

$$260 \quad \bar{C}^{ep}(\sigma) = \begin{bmatrix} C_{11}^{ep} & C_{12}^{ep} \\ C_{21}^{ep} & C_{22}^{ep} \end{bmatrix} \quad (34)$$

261 (matrix \bar{C} is formed analogously), we derive conditions in section 5 such that
 262 $\det \bar{C}^{ep} > 0$, as is required for well-posedness.

263 Specified background stresses in the medium, denoted $\sigma_{xx}^0, \sigma_{yy}^0, \sigma_{zz}^0$ are
 264 depth variable (see section 9), and the initial background shear stresses are
 265 given by σ_{xy}^0 and σ_{xz}^0 . Note that from (30), antiplane deformation can activate
 266 changes in normal stresses (for example, $d\sigma_{xx} = C_{xxxy}^{ep} d\gamma_{xy} + C_{xxxz}^{ep} d\gamma_{xz}$) unless

267 the relevant components of the tangent stiffness tensor are zero. This scenario
 268 can be avoided with the assumption $\beta = 0$ and $\sigma_{xx}^0 = \sigma_{yy}^0 = \sigma_{zz}^0$, which we
 269 make for the rest of this work.

270 In this work we assume isotropic elastic moduli $C_{11} = C_{22} = \mu$, and $C_{12} =$
 271 $C_{21} = 0$. For antiplane strain the specific components for the elastoplastic
 272 stiffness tensor (30) are thus

$$273 \quad C_{11}^{ep} = \begin{cases} \mu & \text{if } \lambda = 0, \\ \mu - \frac{\mu\sigma_{xy}^2/\bar{\tau}^2}{1+h/\mu} & \text{if } \lambda > 0, \end{cases} \quad (35)$$

$$274 \quad C_{22}^{ep} = \begin{cases} \mu & \text{if } \lambda = 0, \\ \mu - \frac{\mu\sigma_{xz}^2/\bar{\tau}^2}{1+h/\mu} & \text{if } \lambda > 0, \end{cases} \quad (36)$$

276 and

$$277 \quad C_{12}^{ep} = C_{21}^{ep} = \begin{cases} 0 & \text{if } \lambda = 0, \\ -\frac{\mu\sigma_{xy}\sigma_{xz}/\bar{\tau}^2}{1+h/\mu} & \text{if } \lambda > 0. \end{cases} \quad (37)$$

278 Note that matrix \bar{C}^{ep} is symmetric and in the antiplane setting, Drucker-
 279 Prager reduces to von-Mises plasticity. Equation (17) reduces to

$$280 \quad \bar{\tau} = \sqrt{\sigma_{xy}^2 + \sigma_{xz}^2} \quad (38)$$

281 and the corresponding flow rule (19) is given by

$$282 \quad \dot{\gamma}_{xy}^p = \lambda \frac{\sigma_{xy}}{\bar{\tau}}, \quad \dot{\gamma}_{xz}^p = \lambda \frac{\sigma_{xz}}{\bar{\tau}}. \quad (39)$$

283 The yield stress (18) reduces to

$$284 \quad \sigma_Y = -(\sigma_{kk}^0/3) \sin \phi + c \cos \phi. \quad (40)$$

285 5. Incremental Energy Balance

286 We now switch from tensor notation used in previous sections to ma-
 287 trix/vector notation, in order to facilitate comparison with the discrete for-
 288 mulation we derive in the next section. We also assume, for ease of the
 289 analysis in the following sections, that the boundary conditions for the in-
 290 cremental problem (33) involve general boundary data dg_L, dg_R, dg_T and dg_B
 291 at the left, right, top and bottom boundaries (respectively) namely,

292 $du(t, 0, z) = dg_L(t, z),$ (41a)

293 $du(t, L_y, z) = dg_R(t, z),$ (41b)

294 $C_{21}^{ep} \frac{\partial du}{\partial y} + C_{22}^{ep} \frac{\partial du}{\partial z} \Big|_{z=0} = dg_T(t, y),$ (41c)

295 $C_{21}^{ep} \frac{\partial du}{\partial y} + C_{22}^{ep} \frac{\partial du}{\partial z} \Big|_{z=L_z} = dg_B(t, y).$ (41d)

296 Later, however, we outline how we specify incremental boundary conditions
 297 so as to impose fault slip, slow tectonic loading and free surface conditions,
 298 as expressed in (7).

299 Assuming the solution to (33) with boundary conditions (41) is sufficiently
 300 smooth, we multiply (33) by the incremental velocity du and integrate by
 301 parts, yielding the following energy balance

302 $\frac{d}{dt} dE = \int_0^{L_z} du d\sigma_{xy} \Big|_0^{L_y} dz + \int_0^{L_y} du d\sigma_{xz} \Big|_0^{L_z} dy,$ (42)

303 where the incremental internal energy is defined by

304 $dE = \frac{1}{2} \int_0^{L_y} \int_0^{L_z} dU^T \bar{C}^{ep}(\sigma) dU dy dz$ (43)

305 for vector

306 $dU = \begin{bmatrix} \partial du / \partial y \\ \partial du / \partial z \end{bmatrix}.$

307 The symmetric 2×2 matrix \bar{C}^{ep} has eigenvalues

308 $\lambda_1, \lambda_2 = \begin{cases} \mu & \text{if } \lambda = 0, \\ \mu, h/(1 + h/\mu) & \text{if } \lambda > 0 \end{cases}$ (44)

309 and (25) implies that $1 + h/\mu > 0$. \bar{C}^{ep} is therefore positive definite for rate-
 310 independent plasticity if and only if $h > 0$ (*Horn and Johnson, 1985*). If
 311 $h < 0$, $\det(\bar{C}^{ep}) = \lambda_1 \lambda_2 \leq 0$, which results in a loss of ellipticity of the equi-
 312 librium equation (33) and a loss of solvability. This case violates Drucker's
 313 first stability postulate (requiring $dU^T \bar{C}^{ep}(\sigma) dU > 0$) and can lead to prob-
 314 lems including loss of uniqueness of the solution (*Drucker, 1959; Jain, 1989*;

315 *Bower*, 2010). For the case $h \leq 0$, the constitutive theory therefore requires
 316 modification (through the introduction of rate dependence, for example).
 317 Thus for rate-independent plasticity, $h > 0$ is required; however, viscosity in
 318 the viscoplastic model ensures a positive definite matrix, even if $h = 0$ (see
 319 section 7.2).

320 Note that in terms of increments, the rate of change of the internal energy
 321 can be decomposed into the sum of the rate of change of the mechanical (elas-
 322 tic strain) energy and the plastic dissipation (a positive quantity), namely,

$$\frac{d}{dt}dE = \frac{d}{dt} \int_0^{L_y} \int_0^{L_z} \frac{1}{2} [dU^e]^T \bar{C} dU^e dy dz + \int_0^{L_y} \int_0^{L_z} [dU^e]^T \bar{C} d\dot{U}^p dy dz, \quad (45)$$

323 where $dU^e = dU - dU^p$, is the vector of elastic strains and the plastic strain
 324 vector is

$$dU^p = \begin{bmatrix} d\gamma_{xy}^p \\ d\gamma_{xz}^p \end{bmatrix}.$$

325
 326
 327 For simplicity in the analysis only (see *Erickson and Dunham* (2014) for
 328 details), we may take the boundary data $dg_L = dg_R = dg_T = dg_B = 0$ and
 329 show that (42) reduces to

$$\frac{d}{dt}dE = 0, \quad (46)$$

330
 331 showing conservation of the incremental internal energy (or dissipation of the
 332 incremental mechanical energy) in the absence of source terms and nontrivial
 333 boundary conditions (i.e., in the absence of work done by body forces or
 334 surface tractions).

335 6. The Spatial Discretization

336 The nonlinearities present in the governing equation (33) with boundary
 337 conditions (41) make analytical solutions difficult, if not impossible to obtain,
 338 except perhaps in certain limiting cases. SBP-SAT finite difference methods
 339 are often used, however, to obtain numerical approximations to solutions
 340 of nonlinear problems (e.g., Navier-Stokes from fluid mechanics (*Nordström*
 341 *et al.*, 2007)), although the stability analysis can be challenging and is gen-
 342 erally approached by consideration of the linearized or “frozen coefficient”
 343 problem. If the solution is sufficiently smooth (which is not guaranteed for
 344 our problem), the linearized analysis is often enough to ensure convergence
 345 for the nonlinear problem (*Gustafsson*, 2008).

346 We discretize equation (33) using the second-order accurate, narrow-
 347 stencil, summation-by-parts (SBP) finite difference operators for second deriva-
 348 tives, originally defined in *Mattsson and Nordström* (2004) for constant co-
 349 efficients, and for variable coefficients in *Mattsson* (2011). Time-dependent
 350 boundary conditions are imposed and the elastoplastic moduli C_{11}^{ep} , C_{12}^{ep} , C_{21}^{ep}
 351 and C_{22}^{ep} are nonlinear functions of the current stress state (or equivalently, of
 352 the displacement increment). We use a Newton’s method with line search to
 353 solve the nonlinear equation, detailed in section 7.3. At each time step, and
 354 each iteration of Newton’s method we consider the moduli as frozen, spatially
 355 variable coefficients, and use the static counterpart of the spatial discretiza-
 356 tion of the anisotropic acoustic wave equation in heterogeneous media (*Virta*
 357 *and Mattsson*, 2014).

358 We apply second-order accurate SBP operators and introduce the 2D
 359 operators by first considering one spatial dimension. The 1D domain $y \in$
 360 $[0, L]$ is discretized into $N_y + 1$ grid points y_0, y_1, \dots, y_{N_y} with grid spacing
 361 $\Delta y = L/N_y$. First derivatives are approximated by $\frac{\partial u}{\partial y} \approx \mathbf{D}\mathbf{u}$, where $\mathbf{u} =$
 362 $[u_0, u_1, \dots, u_{N_y}]^T$ is the grid function and matrix $\mathbf{D} = \mathbf{H}^{-1}\mathbf{Q}$ is an $N_y + 1 \times$
 363 $N_y + 1$ finite difference operator. \mathbf{H} and \mathbf{Q} are also $N_y + 1 \times N_y + 1$ matrices and
 364 the building blocks for the SBP operators. \mathbf{H} is a diagonal, positive definite
 365 quadrature matrix defining a discrete norm on the space of grid functions

$$366 \quad \|\mathbf{u}\|_H^2 = \mathbf{u}^T \mathbf{H} \mathbf{u}, \quad (47)$$

367 and \mathbf{Q} is an almost skew-symmetric matrix such that $\mathbf{Q} + \mathbf{Q}^T = \text{diag}[-1, 0, 0, \dots, 0, 1]$.
 368 The SBP operators are derived such that they mimic integration-by-parts
 369 and provide a discrete energy estimate (that mimics its continuum coun-
 370 terpart). Namely, the relation $\int_0^L u \frac{\partial u}{\partial y} dy = \frac{1}{2} [u^2(L) - u^2(0)]$ is obtained
 371 by integration-by-parts and is mimicked discretely by $\mathbf{u}^T \mathbf{H} (\mathbf{D}\mathbf{u}) = \frac{1}{2} \mathbf{u} (\mathbf{Q} +$
 372 $\mathbf{Q}^T) \mathbf{u} = \frac{1}{2} (u_N^2 - u_0^2)$. If $p(y)$ defines the variable coefficient, the narrow-stencil
 373 second derivative operator for variable coefficients is given by

$$374 \quad \frac{\partial}{\partial y} (p(y) \frac{\partial}{\partial y}) \approx \mathbf{D}_2^p = \mathbf{H}^{-1} (-\mathbf{M}^p + \mathbf{pBS}), \quad (48)$$

375 where $\mathbf{B} = \text{diag}[-1, \dots, 1]$, and \mathbf{S} approximates the first derivative operator
 376 on the boundary. Matrix $\mathbf{M}^p = \mathbf{D}^T \mathbf{H} \mathbf{pD} + \mathbf{R}^p$, where $\mathbf{R}^p = \frac{(\Delta y)^3}{4} (\mathbf{D}_2)^T \mathbf{C}_2 \mathbf{pD}_2$
 377 (correcting the typographical error in equation (21) in *Erickson and Dunham*
 378 (2014)) is a positive definite damping matrix and $\mathbf{C}_2 = \text{diag}[0, 1, 1, \dots, 1, 1, 0]$

379 (*Mattsson, 2011*). Matrix $\mathbf{p} = \text{diag}[p(y_0), p(y_1), \dots, p(y_{N_y})]$ is a $N_y + 1 \times$
 380 $N_y + 1$ coefficient matrix (all coefficient matrices are denoted similarly, with
 381 bold notation).

382 In 2D, we discretize the domain $[0, L_y] \times [0, L_z]$ with an $N_y + 1 \times N_z + 1$ -
 383 point grid, defined by

$$384 \quad y_i = i\Delta y, \quad i = 0, 1, \dots, N_y, \quad \Delta y = L_y/N_y, \quad (49a)$$

$$385 \quad z_i = i\Delta z, \quad i = 0, 1, \dots, N_z, \quad \Delta z = L_z/N_z, \quad (49b)$$

386 where Δy and Δz are the grid spacings in each direction. Thus $u_{i,j} \approx$
 387 $u(y_j, z_i)$. Letting $N = (N_y + 1)(N_z + 1)$, the $N \times 1$ grid vector \mathbf{u} in 2D is
 388 given by

$$389 \quad \mathbf{u} = [\mathbf{u}_0^T, \mathbf{u}_1^T, \dots, \mathbf{u}_{N_y}^T] \quad (50)$$

390 where

$$391 \quad \mathbf{u}_i = [u_{0,i}, u_{1,i}, \dots, u_{N_z,i}], \text{ for } i = 0, \dots, N_y. \quad (51)$$

392 The 2D variable coefficient $p(y, z)$ defined on $[0, L_y] \times [0, L_z]$ is transformed
 393 to the $N \times N$ diagonal matrix $\mathbf{p} = \text{diag}[\mathbf{p}_0^T, \mathbf{p}_1^T, \dots, \mathbf{p}_{N_y}^T]$ using analogous
 394 notation. To form the SBP finite difference operators in 2D we make use of
 395 the Kronecker product. Recall that if matrix \mathbf{A} is size $p \times q$ and \mathbf{B} is $r \times s$
 396 then the Kronecker product of the two is of size $pr \times qs$ and given by

$$397 \quad \mathbf{A} \otimes \mathbf{B} = \begin{bmatrix} a_{0,0}\mathbf{B} & \cdots & a_{0,N}\mathbf{B} \\ \vdots & & \vdots \\ a_{N,0}\mathbf{B} & \cdots & a_{N,N}\mathbf{B} \end{bmatrix}. \quad (52)$$

398 In addition, the following identities hold:

$$399 \quad (\mathbf{A} \otimes \mathbf{B})(\mathbf{C} \otimes \mathbf{D}) = (\mathbf{AC}) \otimes (\mathbf{BD}), \quad (53a)$$

$$400 \quad (\mathbf{A} \otimes \mathbf{B})^{-1} = (\mathbf{A}^{-1} \otimes \mathbf{B}^{-1}) \text{ if } \mathbf{A} \text{ and } \mathbf{B} \text{ are invertible,} \quad (53b)$$

$$401 \quad (\mathbf{A} \otimes \mathbf{B})^T = \mathbf{A}^T \otimes \mathbf{B}^T. \quad (53c)$$

402 We can thus extend any 1D operator \mathbf{P} to 2D (in the y and z direction,
 403 respectively) by

$$404 \quad \mathbf{P}_y = (\mathbf{P} \otimes \mathbf{I}), \quad (54a)$$

$$405 \quad \mathbf{P}_z = (\mathbf{I} \otimes \mathbf{P}). \quad (54b)$$

406 The first and second derivative operators in 2D are thus

$$407 \quad \frac{\partial}{\partial y} \approx \mathbf{D}_y, \quad (55a)$$

$$408 \quad \frac{\partial}{\partial z} \approx \mathbf{D}_z, \quad (55b)$$

$$409 \quad \frac{\partial}{\partial y} \left(p(y, z) \frac{\partial}{\partial y} \right) \approx \mathbf{D}_{2y}^p = \mathbf{H}_y^{-1} [-\mathbf{D}_y^T \mathbf{p} \mathbf{H}_y \mathbf{D}_y - \mathbf{R}_y^p + \mathbf{p} \mathbf{B}_y \mathbf{S}_y], \quad (55c)$$

$$410 \quad \frac{\partial}{\partial z} \left(p(y, z) \frac{\partial}{\partial z} \right) \approx \mathbf{D}_{2z}^p = \mathbf{H}_z^{-1} [-\mathbf{D}_z^T \mathbf{p} \mathbf{H}_z \mathbf{D}_z - \mathbf{R}_z^p + \mathbf{p} \mathbf{B}_z \mathbf{S}_z], \quad (55d)$$

411 where $\mathbf{R}_y^p, \mathbf{R}_z^p$ are positive definite damping matrices in 2D (see *Erickson*
412 *and Dunham* (2014) for details). The equilibrium equation (33), along with
413 boundary conditions (41), is thus discretized by

$$414 \quad \mathbf{D}_{2y}^{\mathbf{C}_{11}^{ep}} \mathbf{d}\mathbf{u} + \mathbf{D}_y \mathbf{C}_{12}^{ep} \mathbf{D}_z \mathbf{d}\mathbf{u} + \mathbf{D}_z \mathbf{C}_{21}^{ep} \mathbf{D}_y \mathbf{d}\mathbf{u} + \mathbf{D}_{2z}^{\mathbf{C}_{22}^{ep}} \mathbf{d}\mathbf{u} + \mathbf{P}_L + \mathbf{P}_R + \mathbf{P}_T + \mathbf{P}_B = \mathbf{0}, \quad (56)$$

415 where $\mathbf{d}\mathbf{u}$ is the incremental displacement grid vector, and the SAT penalty
416 vectors are given by

$$417 \quad \mathbf{P}_L = \mathbf{H}_y^{-1} (\boldsymbol{\alpha}_L + \beta \mathbf{H}_z^{-1} (-\mathbf{C}_{11}^{ep} \mathbf{S}_y - \mathbf{C}_{12}^{ep} \mathbf{D}_z)^T) \mathbf{H}_z \mathbf{E}_0 (\mathbf{d}\mathbf{u}_L - \mathbf{d}\mathbf{g}_L) \quad (57a)$$

$$418 \quad \mathbf{P}_R = \mathbf{H}_y^{-1} (\boldsymbol{\alpha}_R + \beta \mathbf{H}_z^{-1} (\mathbf{C}_{11}^{ep} \mathbf{S}_y + \mathbf{C}_{12}^{ep} \mathbf{D}_z)^T) \mathbf{H}_z \mathbf{E}_N (\mathbf{d}\mathbf{u}_R - \mathbf{d}\mathbf{g}_R) \quad (57b)$$

$$419 \quad \mathbf{P}_T = -\mathbf{H}_z^{-1} (\mathbf{I}_y \otimes \mathbf{E}_0) ([-\mathbf{C}_{22}^{ep} \mathbf{S}_z \mathbf{d}\mathbf{u} - \mathbf{C}_{21}^{ep} \mathbf{D}_y \mathbf{d}\mathbf{u}]_T - \mathbf{d}\mathbf{g}_T) \quad (57c)$$

$$420 \quad \mathbf{P}_B = -\mathbf{H}_z^{-1} (\mathbf{I}_y \otimes \mathbf{E}_N) ([\mathbf{C}_{22}^{ep} \mathbf{S}_z \mathbf{d}\mathbf{u} + \mathbf{C}_{21}^{ep} \mathbf{D}_y \mathbf{d}\mathbf{u}]_B - \mathbf{d}\mathbf{g}_B). \quad (57d)$$

421 Recall that the coefficient matrices in (56) depend nonlinearly on the stress $\boldsymbol{\sigma}$.
422 The notation $\mathbf{d}\mathbf{u}_L$ is the restriction of the grid vector $\mathbf{d}\mathbf{u}$ to the left boundary
423 and $\mathbf{d}\mathbf{u}_R, \mathbf{d}\mathbf{u}_T, \mathbf{d}\mathbf{u}_B$, are the restrictions to the right, top and bottom bound-
424 aries (respectively). Vector $\mathbf{d}\mathbf{g}_L$ is the boundary data dg_L evaluated at the
425 grid and $\mathbf{d}\mathbf{g}_R, \mathbf{d}\mathbf{g}_T, \mathbf{d}\mathbf{g}_B$ are defined analogously. Matrices \mathbf{E}_0 and \mathbf{E}_N map
426 the restricted vectors to full-length ($N \times 1$ length) vectors (see *Erickson and*
427 *Dunham* (2014) for details). *Virta and Mattsson* (2014) derive conditions
428 on the penalty parameter β and penalty matrices $\boldsymbol{\alpha}_L$, and $\boldsymbol{\alpha}_R$ such that a
429 semi-discrete energy estimate can be obtained. Following their analysis, the
430 semi-discrete incremental internal energy $\mathbf{d}\mathbf{E}$ (a slightly modified analog of
431 (43)) is defined

$$432 \quad \mathbf{d}\mathbf{E} = \frac{1}{2} \mathbf{d}\mathbf{U}^T (\mathbf{H}_y \otimes \mathbf{H}_z) \bar{\mathbf{C}}^{ep} \mathbf{d}\mathbf{U} + \frac{1}{2} \mathbf{d}\mathbf{u}^T (\mathbf{R}_y^{\mathbf{C}_{11}^{ep}} \otimes \mathbf{H}_z) \mathbf{d}\mathbf{u} + \frac{1}{2} \mathbf{d}\mathbf{u}^T (\mathbf{H}_y \otimes \mathbf{R}_z^{\mathbf{C}_{22}^{ep}}) \mathbf{d}\mathbf{u} + U_1 + U_2. \quad (58)$$

433 In (58), vector $\mathbf{dU} = [\mathbf{D}_y \mathbf{d}\mathbf{u} \ \mathbf{D}_z \mathbf{d}\mathbf{u}]^T$, the positive-definiteness of the $2N \times$
 434 $2N$, block diagonal matrix

$$435 \quad \bar{\mathbf{C}}^{ep} = \begin{bmatrix} \mathbf{C}_{11}^{ep} & \mathbf{C}_{12}^{ep} \\ \mathbf{C}_{21}^{ep} & \mathbf{C}_{22}^{ep} \end{bmatrix} \quad (59)$$

436 follows from that of $\bar{\mathbf{C}}^{ep}$, and U_1, U_2 are positive quantities, see Appendix
 437 A. Assuming zero-boundary data, as in the continuum problem, the semi-
 438 discrete equations are shown to satisfy the energy estimate

$$439 \quad \frac{d}{dt} \mathbf{dE} \leq 0, \quad (60)$$

440 which ensures stability of the method, see Appendix A for more details. Note
 441 that for our application problems in section 9 we desire better resolution near
 442 the fault and free surface, and therefore consider a non-uniform grid spacing.
 443 In appendix A we detail the stability analysis for a grid with non-uniform
 444 spacing; the uniform grid spacing assumed in this section (to maintain flow
 445 of the discussion) is a special case.

446 7. Time Stepping

447 In this section we explain the time stepping method for the overall prob-
 448 lem. This is done by first updating slip and the state variable along the
 449 frictional fault. The update to slip, along with the remaining boundary con-
 450 ditions, generates an increment of load. Updates to the displacement, stresses
 451 and plastic strains (that occur in the volume in response to the load) are then
 452 computed.

453 We introduce a time discretization so that notationally, superscripts on
 454 a particular field imply we are considering a *finite* increment over a discrete
 455 time step. We assume the system is equilibrated at time t^n with stresses con-
 456 sistent with the constitutive theory of section 3. Slip and state variable along
 457 the fault are updated via a Runge-Kutta method with adaptive time stepping
 458 (see section 7.4 for details). These updates provide the incremental bound-
 459 ary data $\mathbf{d}\mathbf{g}_L^{n+1}$ along the fault, which, together with $\mathbf{d}\mathbf{g}_R^{n+1}, \mathbf{d}\mathbf{g}_T^{n+1}, \mathbf{d}\mathbf{g}_B^{n+1}$,
 460 correspond to an increment of load applied over the time step $dt = t^{n+1} - t^n$
 461 that drives the system to a new state. In what follows, we describe the lat-
 462 ter part update, namely, how the displacement increment and the associated

463 stresses and plastic strains are updated in response to the load in a manner
 464 that accounts for plastic response.

465 Let the discrete equilibrium equation (56)-(57) be denoted $\mathcal{E}(\mathbf{d}\boldsymbol{\sigma}) = \mathbf{b}$
 466 where vector \mathbf{b} stores the incremental boundary data. At t^{n+1} we wish to
 467 obtain both stress and displacement increments that satisfy

$$468 \quad \mathcal{E}(\mathbf{d}\boldsymbol{\sigma}^{n+1}) = \mathbf{b}^{n+1} \quad (61)$$

469 and are consistent with the constitutive theory of section 3, where $\mathbf{d}\boldsymbol{\sigma}^{n+1}$
 470 is related to the displacement increment $\mathbf{d}\mathbf{u}^{n+1}$ through a discrete form of
 471 constitutive relation (31) (which we define shortly) and the discretized strain-
 472 displacement relations (32).

473 To obtain the displacement, stresses and strains at time t^{n+1} we first
 474 apply a backward-Euler discretization to the flow rule (19) and equivalent
 475 plastic strain

$$476 \quad \gamma_{xy}^{p,n+1} = \gamma_{xy}^{p,n} + \mathbf{d}\boldsymbol{\lambda}^{n+1} \frac{\boldsymbol{\sigma}_{xy}^{n+1}}{\bar{\boldsymbol{\tau}}^{n+1}} \quad (62a)$$

$$477 \quad \gamma_{xz}^{p,n+1} = \gamma_{xz}^{p,n} + \mathbf{d}\boldsymbol{\lambda}^{n+1} \frac{\boldsymbol{\sigma}_{xz}^{n+1}}{\bar{\boldsymbol{\tau}}^{n+1}}, \quad (62b)$$

$$478 \quad \gamma^{p,n+1} = \gamma^{p,n} + \mathbf{d}\boldsymbol{\lambda}^{n+1}, \quad (62c)$$

479 where $\mathbf{d}\boldsymbol{\lambda}^{n+1} = \boldsymbol{\lambda}^{n+1} dt$. A direct linearization of this discretization implies
 480 an associated discrete, incremental form of the constitutive relation given by

$$481 \quad \mathbf{d}\boldsymbol{\sigma}_{ij}^{n+1} = \mathbf{C}_{ijkl}^{ep}(\boldsymbol{\sigma}^{n+1}) \mathbf{d}\boldsymbol{\epsilon}_{kl}^{n+1} \quad (63)$$

482 where \mathbf{C}^{ep} is the *consistent* tangent stiffness tensor (and a function of the
 483 stress at the end of the time step), derived in the next section. The fully
 484 discrete equilibrium equation can thus be expressed

$$485 \quad \mathcal{E}(\mathbf{C}^{ep}(\boldsymbol{\sigma}^{n+1}) \mathbf{d}\mathbf{u}^{n+1}) = \mathbf{b}^{n+1}, \quad (64)$$

486 and is a nonlinear function of $\mathbf{d}\mathbf{u}^{n+1}$.

487 To solve (64) we proceed via a Newton-type method which utilizes the
 488 partial derivative

$$489 \quad \frac{\partial \mathcal{E}}{\partial \mathbf{d}\mathbf{u}^{n+1}} = \frac{\partial \mathcal{E}}{\partial \mathbf{d}\boldsymbol{\sigma}_{ij}^{n+1}} \mathbf{C}_{ijkl}^{ep}(\boldsymbol{\sigma}^{n+1}) \frac{\partial \mathbf{d}\boldsymbol{\epsilon}_{kl}^{n+1}}{\partial \mathbf{d}\mathbf{u}^{n+1}} \quad (65)$$

490 and incorporates the consistent tangent stiffness tensor. We set iteration
 491 index $k = 0$ and compute an initial, elastic guess $\mathbf{du}^{n+1,(k)}$ to the displace-
 492 ment increment, obtained by assuming $\mathcal{C}^{ep} = \mathbf{C}$ and solving (64). Consistent
 493 stresses $\boldsymbol{\sigma}^{n+1,(k)}$ associated with $\mathbf{du}^{n+1,(k)}$ are obtained from the *return map-*
 494 *ping algorithm* which is based on the backward Euler discretization (62), and
 495 detailed in the next section. Deferring specific details until section 7.4, if
 496 the new, consistent stress state satisfies equilibrium, then the final fields are
 497 those at iteration k , and the process is considered done.

498 If equilibrium is not satisfied, however, the displacement increment $\mathbf{du}^{n+1,(k)}$
 499 must be adjusted (and thus adjustments to the stress and plastic strains must
 500 be made). The displacement increment is updated by solving (64) via an it-
 501 erative Newton-type method that solves the *linearized* equilibrium problem

$$502 \quad \mathcal{E}(\mathcal{C}^{ep}(\boldsymbol{\sigma}^{n+1,(k)})\mathbf{du}^{n+1,(k+1)}) = \mathbf{b}^{n+1}. \quad (66)$$

503 and the return mapping algorithm provides associated consistent stresses
 504 $\boldsymbol{\sigma}^{n+1,(k+1)}$ (*Simo and Hughes, 1998; de Souza Neto et al., 2008*). This iterative
 505 procedure continues until equilibrium has been satisfied with an appropriate
 506 convergence criterion met (see section 7.3). The displacement $\mathbf{u}^{n+1} = \mathbf{u}^n +$
 507 \mathbf{du}^{n+1} can then be formed from the converged value of the finite increment
 508 \mathbf{du}^{n+1} .

509 7.1. The Return Mapping Algorithm

510 Within the Newton iteration described in the previous section, the finite
 511 displacement increment $\mathbf{du}^{n+1,(k)}$ is obtained and stresses consistent with the
 512 plastic constitutive theory must be updated (*Simo and Hughes, 1998*). In
 513 this section we describe how to obtain $\boldsymbol{\sigma}^{n+1,(k)}$. First, the strains associated
 514 with $\mathbf{du}^{n+1,(k)}$ are computed

$$515 \quad \boldsymbol{\gamma}_{xy}^{n+1,(k)} = \boldsymbol{\gamma}_{xy}^n + \mathbf{d}\boldsymbol{\gamma}_{xy}^{n+1,(k)}, \quad (67a)$$

$$516 \quad \boldsymbol{\gamma}_{xz}^{n+1,(k)} = \boldsymbol{\gamma}_{xz}^n + \mathbf{d}\boldsymbol{\gamma}_{xz}^{n+1,(k)}, \quad (67b)$$

517 and allow us to compute the elastic trial state (denoted with asterisk *)

$$518 \quad \boldsymbol{\gamma}^{*,p,n+1,(k)} = \boldsymbol{\gamma}^{p,n}, \quad (68a)$$

$$519 \quad \boldsymbol{\sigma}_{xz}^{*,n+1,(k)} = \mu(\boldsymbol{\gamma}_{xz}^{n+1,(k)} - \boldsymbol{\gamma}_{xz}^{p,n}) = \boldsymbol{\sigma}_{xz}^n + \mu\mathbf{d}\boldsymbol{\gamma}_{xz}^{n+1,(k)}, \quad (68b)$$

$$520 \quad \boldsymbol{\sigma}_{xy}^{*,n+1,(k)} = \mu(\boldsymbol{\gamma}_{xy}^{n+1,(k)} - \boldsymbol{\gamma}_{xy}^{p,n}) = \boldsymbol{\sigma}_{xy}^n + \mu\mathbf{d}\boldsymbol{\gamma}_{xy}^{n+1,(k)}, \quad (68c)$$

521 assuming no additional plastic strain has accrued over the time step.

522 The final stress state at time t^{n+1} must satisfy $F \leq 0$, where the yield
 523 function is defined in (15) for yield stress (40). If the elastic trial stresses sat-
 524 isfy $F \leq 0$, then they are accepted as the final stresses. If the trial stresses lie
 525 outside the yield surface ($F > 0$), however, they are be “mapped back” onto
 526 the yield surface by adjusting the plastic strains so that $F(\boldsymbol{\sigma}^{n+1}, (k), \boldsymbol{\gamma}^{p,n+1,(k)}) =$
 527 0 is satisfied (*Simo and Hughes, 1998*).

528 Substituting equations (62a-b) into (68b-c) yields

$$529 \quad \boldsymbol{\sigma}_{xy}^{*,n+1} = \boldsymbol{\sigma}_{xy}^{n+1}(1 + \mu \mathbf{d}\boldsymbol{\lambda}^{n+1} / \bar{\boldsymbol{\tau}}^{n+1}) \quad (69a)$$

$$530 \quad \boldsymbol{\sigma}_{xz}^{*,n+1} = \boldsymbol{\sigma}_{xz}^{n+1}(1 + \mu \mathbf{d}\boldsymbol{\lambda}^{n+1} / \bar{\boldsymbol{\tau}}^{n+1}). \quad (69b)$$

531 From (69) we calculate

$$532 \quad \begin{aligned} \bar{\boldsymbol{\tau}}^{*,n+1} &= \sqrt{(\boldsymbol{\sigma}_{xy}^{*,n+1})^2 + (\boldsymbol{\sigma}_{xz}^{*,n+1})^2} \\ 533 \quad &= \bar{\boldsymbol{\tau}}^{n+1} + \mu \mathbf{d}\boldsymbol{\lambda}^{n+1}. \end{aligned} \quad (70)$$

534 Re-arranging (70), noting that $F(\boldsymbol{\sigma}^{n+1}, \boldsymbol{\gamma}^{p,n+1}) = 0$, and substituting in (62c)
 535 yields the plastic consistency condition

$$536 \quad \mathbf{d}\boldsymbol{\lambda}^{n+1} = F(\boldsymbol{\sigma}^{*,n+1}, \boldsymbol{\gamma}^{*,p,n+1}) / (h + \mu), \quad (71)$$

537 where $\boldsymbol{\gamma}^{*,p,n+1}$ is given by (68c). Finally, solving (69) for $\boldsymbol{\sigma}_{xy}^{n+1}$ and $\boldsymbol{\sigma}_{xz}^{n+1}$
 538 yields

$$539 \quad \boldsymbol{\sigma}_{xy}^{n+1,(k)} = \frac{\boldsymbol{\sigma}_{xy}^{*,n+1,(k)}}{1 + \mu \mathbf{d}\boldsymbol{\lambda}^{n+1,(k)} / \bar{\boldsymbol{\tau}}^{n+1}} = \frac{\boldsymbol{\sigma}_{xy}^{*,n+1,(k)} (\bar{\boldsymbol{\tau}}^{*,n+1,(k)} - \mu \mathbf{d}\boldsymbol{\lambda}^{n+1,(k)})}{\bar{\boldsymbol{\tau}}^{*,n+1,(k)}} \quad (72a)$$

$$540 \quad \boldsymbol{\sigma}_{xz}^{n+1,(k)} = \frac{\boldsymbol{\sigma}_{xz}^{*,n+1,(k)}}{1 + \mu \mathbf{d}\boldsymbol{\lambda}^{n+1,(k)} / \bar{\boldsymbol{\tau}}^{n+1,(k)}} = \frac{\boldsymbol{\sigma}_{xz}^{*,n+1,(k)} (\bar{\boldsymbol{\tau}}^{*,n+1,(k)} - \mu \mathbf{d}\boldsymbol{\lambda}^{n+1,(k)})}{\bar{\boldsymbol{\tau}}^{*,n+1,(k)}} \quad (72b)$$

541 which expresses the final stress state entirely in terms of the computed elastic
 542 trial stresses.

543 The consistent elastoplastic tangent stiffness tensor \mathbf{C}_{ijkl}^{ep} in (64) is ob-
 544 tained by a linearization of the return-mapping algorithm. We derive these
 545 consistent moduli in Appendix B, with specific components (ommitting su-
 546 perscripts $n + 1$) given by (bold face notation is not used as these moduli are
 547 derived independently of a spatial discretization)

$$548 \quad \mathbf{C}_{11}^{ep} = \begin{cases} \mu & \text{if } \lambda = 0, \\ \mu - \frac{\mu \sigma_{xy}^2 / \bar{\boldsymbol{\tau}}^2}{1 + h / \mu} - \frac{d\lambda \mu^2}{\bar{\boldsymbol{\tau}}} \left[1 - \left(\frac{\sigma_{xy}}{\bar{\boldsymbol{\tau}}} \right)^2 \right] & \text{if } \lambda > 0, \end{cases} \quad (73)$$

549

$$\mathcal{C}_{22}^{ep} = \begin{cases} \mu & \text{if } \lambda = 0, \\ \mu - \frac{\mu\sigma_{xz}^2/\bar{\tau}^2}{1+h/\mu} - \frac{d\lambda\mu^2}{\bar{\tau}} \left[1 - \left(\frac{\sigma_{xz}}{\bar{\tau}} \right)^2 \right] & \text{if } \lambda > 0, \end{cases} \quad (74)$$

551 and

$$\mathcal{C}_{12}^{ep} = \mathcal{C}_{21}^{ep} = \begin{cases} 0 & \text{if } \lambda = 0, \\ -\frac{\mu\sigma_{xy}\sigma_{xz}/\bar{\tau}^2}{1+h/\mu} - \frac{d\lambda\mu^2}{\bar{\tau}} \left[1 - \frac{\sigma_{xy}\sigma_{xz}}{\bar{\tau}^2} \right] & \text{if } \lambda > 0, \end{cases} \quad (75)$$

553 which agree with the continuum moduli in the limit that $d\lambda \rightarrow 0$.

554 It has been shown for many problems that using the consistent tangent
555 moduli (73)-(75) with discretization (64) (to compute numerical solutions
556 to (33)) then the quadratic convergence rate typical of Newton-type itera-
557 tive methods is achieved. This rate of convergence is often lost, however, if
558 the continuum tangent moduli (35)-(37) are used instead (*Simo and Taylor*,
559 1985). In our application problems we thus use the consistent elastoplastic
560 moduli and leave the comparison of Newton convergence results to future
561 work.

562 *7.2. Extension to Viscoplasticity*

563 Classical Perzyna viscoplasticity (*Perzyna*, 1966, 1971) is obtained from
564 rate-independent plasticity by replacing the yield condition (16) with $F(\boldsymbol{\sigma}, \boldsymbol{\gamma}^p) =$
565 $\eta\boldsymbol{\lambda}$, where $\eta > 0$ is the viscosity. A viscoplastic response alters the return
566 mapping algorithm in the previous section through the following: If the
567 computed elastic trial stresses are such that $F(\boldsymbol{\sigma}^{*,n+1}, \boldsymbol{\gamma}^{*,p,n+1}) > 0$, then
568 equations (70) and (71) are replaced with

$$\bar{\tau}^{*,n+1} = \bar{\tau}^{n+1} + \mu \frac{F^{n+1}}{\eta} dt \quad (76)$$

570 and

$$d\boldsymbol{\lambda}^{n+1} = F(\boldsymbol{\sigma}^{*,n+1}, \boldsymbol{\gamma}^{*,p,n+1}) / (\eta/dt + h + \mu). \quad (77)$$

572 The consistent elastoplastic tangent moduli (73)-(75) can also be derived
573 from linearizing the return-mapping algorithm (see Appendix B), yielding

$$\mathcal{C}_{11}^{ep} = \begin{cases} \mu & \text{if } \boldsymbol{\lambda} = 0, \\ \mu - \frac{\mu\sigma_{xy}^2/\bar{\tau}^2}{\frac{\eta/\mu}{dt} + 1 + h/\mu} - \frac{d\lambda\mu^2}{\bar{\tau}} \left[1 - \left(\frac{\sigma_{xy}}{\bar{\tau}} \right)^2 \right] & \text{if } \boldsymbol{\lambda} > 0, \end{cases} \quad (78)$$

$$\mathcal{C}_{22}^{ep} = \begin{cases} \mu & \text{if } \lambda = 0, \\ \mu - \frac{\mu\sigma_{xz}^2/\bar{\tau}^2}{\frac{\eta/\mu}{dt} + 1 + h/\mu} - \frac{d\lambda\mu^2}{\bar{\tau}} \left[1 - \left(\frac{\sigma_{xz}}{\bar{\tau}} \right)^2 \right] & \text{if } \lambda > 0, \end{cases} \quad (79)$$

574 and

$$\mathcal{C}_{12}^{ep} = \mathcal{C}_{21}^{ep} = \begin{cases} 0 & \text{if } \lambda = 0, \\ -\frac{\mu\sigma_{xy}\sigma_{xz}/\bar{\tau}^2}{\frac{\eta/\mu}{dt} + 1 + h/\mu} - \frac{d\lambda\mu^2}{\bar{\tau}} \left[1 - \frac{\sigma_{xy}\sigma_{xz}}{\bar{\tau}^2} \right] & \text{if } \lambda > 0. \end{cases} \quad (80)$$

575 Note that for a fixed η , if $dt \rightarrow 0$, the consistent elastoplastic moduli (78) -
 576 (80) approach the elastic moduli. Furthermore, for $\eta > 0$, we can take $h = 0$
 577 and still guarantee that $\bar{\mathcal{C}}^{ep}$ is positive definite.

578 7.3. Newton Iteration with Return-Mapping

579 We let $k = 0$, $\mathbf{du}^{n+1,(k)}$ be the initial (elastic) guess for the displacement
 580 increment \mathbf{du}^{n+1} , and iterate as follows.

581 Step 1: Compute the strain increments

$$582 \quad \mathbf{d}\boldsymbol{\gamma}_{xy}^{n+1,(k)} = \mathbf{D}_y \mathbf{du}^{n+1,(k)}, \quad (81a)$$

$$583 \quad \mathbf{d}\boldsymbol{\gamma}_{xz}^{n+1,(k)} = \mathbf{D}_z \mathbf{du}^{n+1,(k)}. \quad (81b)$$

584 Step 2: Compute the elastic trial state and use the return mapping algorithm
 585 to obtain the consistent stresses $\boldsymbol{\sigma}_{xy}^{n+1,(k)}$, $\boldsymbol{\sigma}_{xz}^{n+1,(k)}$ and plastic strain $\boldsymbol{\gamma}^{p,n+1,(k)}$.

586 Step 3: Check if equilibrium is sufficiently satisfied. That is, check if a
 587 stopping criterion is met, for example, $\|\boldsymbol{\mathcal{E}}(\mathcal{C}^{ep}(\boldsymbol{\sigma}^{n+1,(k)})\mathbf{du}^{n+1,(k)}) - \mathbf{b}^{n+1}\| <$
 588 tol , where tol is a specified tolerance. If so, set $\mathbf{u}^{n+1} = \mathbf{u}^n + \mathbf{du}^{n+1,(k)}$,
 589 the remaining fields are those at iteration (k), and the Newton iteration
 590 is complete. Otherwise set $k = k + 1$, solve $\boldsymbol{\mathcal{E}}(\mathcal{C}^{ep}(\boldsymbol{\sigma}^{n+1,(k)})\mathbf{du}^{n+1,(k+1)}) =$
 591 \mathbf{b}^{n+1} for $\mathbf{du}^{n+1,(k+1)}$ and return to step 1, iterating until the Newton method
 592 converges and equilibrium is met.

593 7.4. Time Stepping Method

594 In this section we provide details of time stepping for the overall prob-
 595 lem, which includes details of the update to slip and the state variable along
 596 the fault, and provides an initial guess for the off-fault fields. As stated in
 597 section 2, rate-and-state friction, as used in our algorithm, provides the set
 598 of differential equations (9)-(11) that are used to evolve the fault boundary
 599 displacement (i.e., fault slip). We modify the method from *Erickson and*
 600 *Dunham* (2014) in order to incorporate off-fault plasticity. Bold-face type is

601 again used to denote spatially discrete quantities. We assume the body is
 602 equilibrated (with consistent stresses) at time t^n and that \mathbf{V}^n and $\boldsymbol{\psi}^n$ are
 603 known. The following time-stepping method is illustrated in the context of a
 604 forward Euler step, but we use Matlab's adaptive, fourth order Runge-Kutta
 605 method with a relative tolerance of 10^{-7} .

606

607 Step 1. Update slip and state on the fault by explicitly integrating

$$608 \quad \Delta \mathbf{u}^{n+1} = \Delta \mathbf{u}^n + dt \mathbf{V}^n \quad (82a)$$

$$609 \quad \boldsymbol{\psi}^{n+1} = \boldsymbol{\psi}^n + dt G(\mathbf{V}^n, \boldsymbol{\psi}^n). \quad (82b)$$

Step 2. Set the boundary data in (41):

$$\begin{aligned} \mathbf{d}\mathbf{g}_L^{n+1} &= dt \mathbf{V}^n / 2, \\ \mathbf{d}\mathbf{g}_R^{n+1} &= dt V_p / 2, \\ \mathbf{d}\mathbf{g}_T^{n+1} &= \mathbf{d}\mathbf{g}_B^{n+1} = 0, \end{aligned}$$

610 form \mathbf{b}^{n+1} and solve for an elastic increment $\mathbf{d}\mathbf{u}^{n+1,(0)}$; i.e., take $\mathbf{C}^{ep} = \mathbf{C}$ and
 611 solve the discrete equation (64).

612

613 Step 3. Correct the initial elastic guess $\mathbf{d}\mathbf{u}^{n+1,(0)}$ by iterating following the
 614 Newton procedure in section 7.3 until convergence is reached, thus obtaining
 615 $\mathbf{u}^{n+1}, \boldsymbol{\sigma}_{xy}^{n+1}, \boldsymbol{\sigma}_{xz}^{n+1}, \boldsymbol{\gamma}_{xy}^{p,n+1}, \boldsymbol{\gamma}_{xz}^{p,n+1}, \boldsymbol{\gamma}^{p,n+1}$.

616

617 Step 4. Compute the shear stress $\boldsymbol{\tau}_{qs}^{n+1} = \boldsymbol{\sigma}_{xy}^{n+1}|_{y=0}$ on the fault.

618

619 Step 5. Equate shear stress with frictional strength $\boldsymbol{\tau}_{qs}^{n+1} - \eta_{rad} \mathbf{V}^{n+1} =$
 620 $\boldsymbol{\sigma}_n f(\mathbf{V}^{n+1}, \boldsymbol{\psi}^{n+1})$ and solve for the updated slip velocity \mathbf{V}^{n+1} (solved using
 621 a local, safe-guarded Newton method) and return to step 1.

622 8. Convergence Tests and Comparison with Finite Element Solu- 623 tion

624 We conduct two studies to verify our numerical method. The first study
 625 is a convergence test of our spatial discretization and time-stepping for an
 626 elastic problem; the second study is a comparison test with a finite element
 627 solution for the same plasticity model.

628 For the first study we proceed with the method of manufactured solutions
629 and show that our numerical solution is converging to the exact solution at
630 the correct rate (*Roache*, 1998). The nonlinearity introduced by plasticity
631 makes this procedure difficult, thus we solve the anisotropic elastic version
632 by assuming that the elastoplastic moduli do not vary with stress or time,
633 but rather in space only. We want to check that our incremental procedure
634 will provide a numerical approximation to the exact solution to the non-
635 incremental equilibrium equation

$$\frac{\partial}{\partial y} \left[C_{11}^{ep}(y, z) \frac{\partial u}{\partial y} + C_{12}^{ep}(y, z) \frac{\partial u}{\partial z} \right] + \frac{\partial}{\partial z} \left[C_{21}^{ep}(y, z) \frac{\partial u}{\partial y} + C_{22}^{ep}(y, z) \frac{\partial u}{\partial z} \right] = 0, \quad (83)$$

636 where the moduli in (83) are known functions of space. Let the exact displace-
637 ment (denoted with a hat) to (83) be that given in *Erickson and Dunham*
638 (2014), namely
639

$$\hat{u}(t, y, z) = \frac{\delta}{2} K(t) \Phi(y, z) + \frac{V_p t}{2} [1 - \Phi(y, z)] + \frac{\tau^\infty}{\mu} y, \quad (84)$$

641 which provides the exact (elastic) stresses (also denoted with hats)

$$\hat{\sigma}_{xy} = C_{11}^{ep}(y, z) \partial \hat{u} / \partial y + C_{12}^{ep}(y, z) \partial \hat{u} / \partial z \quad (85a)$$

$$\hat{\sigma}_{xz} = C_{21}^{ep}(y, z) \partial \hat{u} / \partial y + C_{22}^{ep}(y, z) \partial \hat{u} / \partial z. \quad (85b)$$

644 Appropriate source terms are added to (83) so that \hat{u} is indeed the solu-
645 tion. In the construction of the exact solution (84), $K(t)$ controls the time-
646 dependency of the solution, δ is the total slip that occurs during the event,
647 τ^∞ is a parameter that defines the remote stress, and Φ describes the spatial
648 dependency of the solution. The specific forms are given by

$$\delta = V_p \bar{t} + V_{\min} \bar{t}, \quad (86a)$$

$$K(t) = \frac{1}{\pi} \left[\tan^{-1} \left(\frac{t - \bar{t}}{t_w} \right) + \frac{\pi}{2} \right] + \frac{V_{\min}}{\delta}, \quad (86b)$$

$$\Phi(y, z) = \frac{H(H + y)}{(H + y)^2 + z^2}, \quad (86c)$$

652 where \bar{t} denotes the event time, t_w denotes the time scale over which the event
653 occurs, V_{\min} defines a minimum slip velocity throughout the simulation, and

654 H defines a locking depth. For the elastic moduli, we assume the following
 655 forms

$$656 \quad C_{11}^{ep} = \mu - \frac{\mu c_1(y, z)^2 / |c|^2}{1 + h/\mu}, \quad (87a)$$

$$657 \quad C_{22}^{ep} = \mu - \frac{\mu c_2(y, z)^2 / |c|^2}{1 + h/\mu}, \quad (87b)$$

$$658 \quad C_{12}^{ep} = C_{21}^{ep} = -\frac{\mu c_1(y, z) c_2(y, z) / |c|^2}{1 + h/\mu}, \quad (87c)$$

659 where

$$660 \quad c_1(y, z) = \frac{H_1^2}{H_1^2 + z^2} \frac{L_1^2}{L_1^2 + y^2}, \quad (88a)$$

$$661 \quad c_2(y, z) = \frac{H_2^2}{H_2^2 + z^2} \frac{L_2^2}{L_2^2 + y^2} \quad (88b)$$

662 and $|c|^2 = c_1^2 + c_2^2$. Thus the moduli form a symmetric, positive definite
 663 matrix \bar{C}^{ep} if $h > 0$. The exact slip along the fault is

$$664 \quad \Delta \hat{u}(t, z) = 2\hat{u}(t, 0, z) = \delta K(t) \Phi(0, z) + V_p t [1 - \Phi(0, z)], \quad (89)$$

665 with slip velocity

$$666 \quad \hat{V}(t, z) = \frac{\partial u^*}{\partial t} \Big|_{y=0^+} - \frac{\partial u^*}{\partial t} \Big|_{y=0^-} = \delta K'(t) \Phi(y, z) + V_p [1 - \Phi(0, z)]. \quad (90)$$

667 Lastly, since $\hat{\tau}(t, z) = \hat{\sigma}_{xy}(t, 0, z)$, we can solve (8) for the exact state variable

$$668 \quad \hat{\psi} = a \ln \left[\frac{2V_0}{\hat{V}} \sinh \left(\frac{\hat{\tau} - \eta_{rad} \hat{V}}{\sigma_n a} \right) \right] \quad (91)$$

669 which implies that a source term must also be added to state evolution

$$670 \quad \dot{\psi} = G(V, \psi) + s(t, z) \quad (92)$$

671 where

$$672 \quad s = \dot{\hat{\psi}} - G(\hat{V}, \hat{\psi}). \quad (93)$$

673 All parameter values used in the convergence tests are given in Table 1.
 674 At the end of the simulation ($t_f = 70$ years), we compute the relative error

Table 1: Parameters used in the manufactured solution convergence tests.

Parameter	Definition	Value
L_z	fault length	24 km
L_y	off-fault domain length	24 km
ℓ_Z	z-length scale for coordinate transform	5 km
ℓ_Y	y-length scale for coordinate transform	5 km
H	locking depth	14 km
L_1	y -length scale for c_1	5 km
H_1	z -length scale for c_1	6 km
L_2	y -length scale for c_2	4 km
H_2	z -length scale for c_2	5 km
ρ	density	2670 kg/m ³
μ	shear modulus	30 GPa
h	hardening modulus	30 GPa
σ_n	normal stress on fault	50 MPa
τ^∞	remote shear stress	40 MPa
t_f	final simulation time	70 years
\bar{t}	event nucleation time	35 years
t_w	timescale for event duration	10 s
a	rate-and-state parameter	0.015
b	rate-and-state parameter	0.02
D_c	critical slip distance	0.4 m
V_p	plate rate	10 ⁻⁹ m/s
V_0	reference velocity	10 ⁻⁶ m/s
f_0	reference friction coefficient	0.6

Table 2: Relative error in the discrete \mathbf{H} - and energy-norms with $N = N_x = N_y$. The rate of convergence approaches 2, as expected for a method with second-order accuracy.

N	$\text{Error}_H(h)$	Rate	$\text{Error}_E(h)$	Rate
2^4	1.030×10^{-3}	–	1.236×10^{-3}	–
2^5	2.867×10^{-4}	1.845	3.514×10^{-4}	1.814
2^6	7.433×10^{-5}	1.947	9.242×10^{-5}	1.927
2^7	1.883×10^{-5}	1.981	2.360×10^{-5}	1.970
2^8	4.741×10^{-6}	1.990	5.967×10^{-6}	1.984

675 between the exact and the numerical approximation in both the discrete
 676 H -norm and the energy-norm, defined by

$$677 \quad \text{Error}_H(h) = \|\mathbf{u} - \hat{\mathbf{u}}\|_H / \|\hat{\mathbf{u}}\|_H \quad (94a)$$

$$678 \quad \text{Error}_E(h) = \|\mathbf{u} - \hat{\mathbf{u}}\|_E / \|\hat{\mathbf{u}}\|_E \quad (94b)$$

679 where

$$680 \quad \|\mathbf{u}\|_H^2 = \sum_{i=1}^M \|\mathbf{d}\mathbf{u}_i\|_H^2 \quad (95a)$$

$$681 \quad \|\mathbf{u}\|_E^2 = \sum_{i=1}^M \mathbf{d}\mathbf{E}_i \quad (95b)$$

682 where $\|\mathbf{d}\mathbf{u}\|_H^2 = (\mathbf{d}\mathbf{u})^T (\mathbf{H}_y \otimes \mathbf{H}_z) (\mathbf{d}\mathbf{u})$, M is the number of adaptive, Runge-
 683 Kutta time steps and $\mathbf{d}\mathbf{E}$ is the incremental internal energy defined by (58).
 684 Table 2 shows that we are achieving second-order convergence, as expected.

685 Because this first verification study confirmed convergence for an anisotropic
 686 elastic problem, the purpose of the next study is to validate our results with
 687 plasticity. For the second validation study, we compare results of the solution
 688 to a boundary value problem subject to Drucker-Prager plasticity. Results
 689 from our finite difference code are compared to those from a finite element
 690 solution using the OpenSees Software Framework (*Mazzoni et al.*, 2009) and
 691 available at <http://opensees.berkeley.edu>.

692 We want to confirm that our incremental approach using equation (33)
 693 (in the context of the time stepping method outlined in the previous section)
 694 solves the non-incremental form of the governing equation (1), on the domain

695 $(y, z) \in [0, L] \times [0, L]$ with boundary conditions given by

$$696 \quad u(0, z) = 0 \quad (96a)$$

$$697 \quad u(L, z) = g(z) \quad (96b)$$

$$698 \quad \sigma_{xz}(y, 0) = 0 \quad (96c)$$

$$699 \quad \sigma_{xz}(y, L) = 0. \quad (96d)$$

700 Boundary data $g(z)$ and all parameter values are listed in Table 3. Stresses
701 are subject to the Drucker-Prager yield condition (15) with constant yield
702 stress σ_Y . We assume an equal grid spacing $\Delta = \Delta y = \Delta z$ of both 1 km
703 ($N_y = N_z = 24$) and 200 m ($N_y = N_z = 120$). Figure 3 shows solutions
704 from the finite difference solution to the plastic boundary value problem
705 with $\Delta = 200$ m, along with the elastic counterpart of the same boundary
706 value problem, in order to illustrate the differences between the two mate-
707 rial models. Figure 3(a-c) show the displacement and two relevant stress
708 components of the plastic solution (in dashed lines) and the elastic solution
709 (solid lines) at different z -values. Figure 3(d-f) are the equivalent fields at
710 various y -values. Although plasticity mildly affects the displacement field,
711 the stresses are significantly reduced in amplitude, particularly near $x = 24$
712 km. Fig. 4 compares contours from the finite difference and finite element
713 solution with $\Delta = 1$ km. The finite difference solution is plotted in solid
714 colors, while the finite element solution is plotted with black circles. The
715 displacement fields in Fig. 4(a-b) are quite similar, but error is visible in the
716 computed stresses, particularly in Fig. 4(d) near $y = 24$ km. This error is
717 visibly decreased when mesh refining, as shown in Figure 5. Absolute and rel-
718 ative errors between the computed fields using the two methods are denoted
719 by $\text{err}_u^a = \|\mathbf{u}^{FD} - \mathbf{u}^{FE}\|_2$ and $\text{err}_u^r = \|\mathbf{u}^{FD} - \mathbf{u}^{FE}\|_2 / \|\mathbf{u}^{FE}\|_2$, respectively,
720 and errors for other fields are defined analogously. Results shown in Table 4
721 suggest the two methods produce similar results.

722 9. Application

723 We are interested in how changes in viscosity, isotropic hardening and
724 cohesion affect features of the earthquake cycle. We find that all three pa-
725 rameters influence the magnitude and off-fault extent of plastic strain, and
726 that in all cases, plasticity affects the amount of slip on the fault in the
727 shallow sub-surface during each rupture. We use the combined spatial dis-
728 cretization and time-stepping method detailed in previous sections to sim-

Table 3: Parameters used in antiplane plastic case for comparison of FDM and FEM.

Parameter	Definition	Value
L_z	fault length	24 km
L_y	off-fault domain length	24 km
μ	shear modulus	32.038 GPa
ρ	material density	2670 kg/m ³
$g(z)$	right boundary condition	$-\cos(\pi z/12) + 1$ (m)
σ_Y	yield stress	4 MPa
ϕ	angle of internal friction	0
h	hardening modulus	32.038 GPa

Table 4: Absolute and relative error between our finite difference solution and that obtained from the finite element code in the discrete L^2 -norm for $N_y = N_z = 24, 120$.

N	err_u^a	err_u^r	$\text{err}_{\sigma_{xy}}^a$	$\text{err}_{\sigma_{xy}}^r$	$\text{err}_{\sigma_{xx}}^a$	$\text{err}_{\sigma_{xz}}^r$
24	1.06×10^0	3.27×10^{-2}	1.72×10^0	3.72×10^{-2}	4.76×10^{-2}	3.22×10^{-2}
120	9.87×10^{-2}	3.04×10^{-3}	1.92×10^{-1}	4.14×10^{-3}	3.81×10^{-3}	2.70×10^{-4}

729 ulate multiple earthquake cycles with off-fault plasticity. The fault is gov-
730 erned by rate-and-state friction with depth-variable parameters a and b (see
731 Fig. 6a). Where $a - b < 0$ defines the velocity-weakening (seismogenic)
732 zone, below which the fault creeps interseismically. As an initial study,
733 we assume that the effective normal stresses in the medium are given by
734 $\sigma_{xx}^0 = \sigma_{yy}^0 = \sigma_{zz}^0 = -(\rho - \rho_w)gz + P_{atm}$ where ρ_w is the density of water, g
735 is the acceleration due to gravity and atmospheric pressure P_{atm} is set to 0.1
736 MPa. The yield stress (15) is thus linearly increasing with depth, see Figure
737 6b. We assume the pore-pressure in the fault is higher than in the surround-
738 ing rock so that although the effective stresses off the fault are depth-variable,
739 effective normal stress on the fault is constant below some depth, see Fig-
740 ure 6b (*Rice, 1992*). Fixing the internal friction parameter ϕ sets the slope
741 of the yield stress and the yield stress at Earth’s surface can be increased
742 or decreased by changing the value of the cohesion c , which we assume is
743 constant with depth. We vary cohesion between 40 and 50 MPa, which are
744 reasonable depth-averaged values of those derived from Hoek-Brown param-
745 eters for many rock strength models (*Roten et al., 2016*). The parameters
746 we use in our simulations are given in Table 5.

747 To determine grid spacing for our application simulations, *Ranjith (2008)*

Table 5: Parameters used in application simulations.

Parameter	Definition	Value
L_z	fault length	24 km
L_y	off-fault domain length	24 km
μ	shear modulus	36 GPa
ρ	density	2800 kg/m ³
c_s	shear wave speed	3.586 km/s
ρ_w	density of water	1000 kg/m ³
σ_n	normal stress on fault	depth-variable
τ^∞	remote shear stress	10 ⁻⁷ MPa
a	rate-and-state parameter	depth-variable
b	rate-and-state parameter	depth-variable
D_c	critical slip distance	8 mm
V_p	plate rate	10 ⁻⁹ m/s
V_0	reference velocity	10 ⁻⁶ m/s
f_0	reference friction coefficient	0.6
c	cohesion	variable
h	hardening modulus	variable
ϕ	internal friction angle	arctan(0.6)

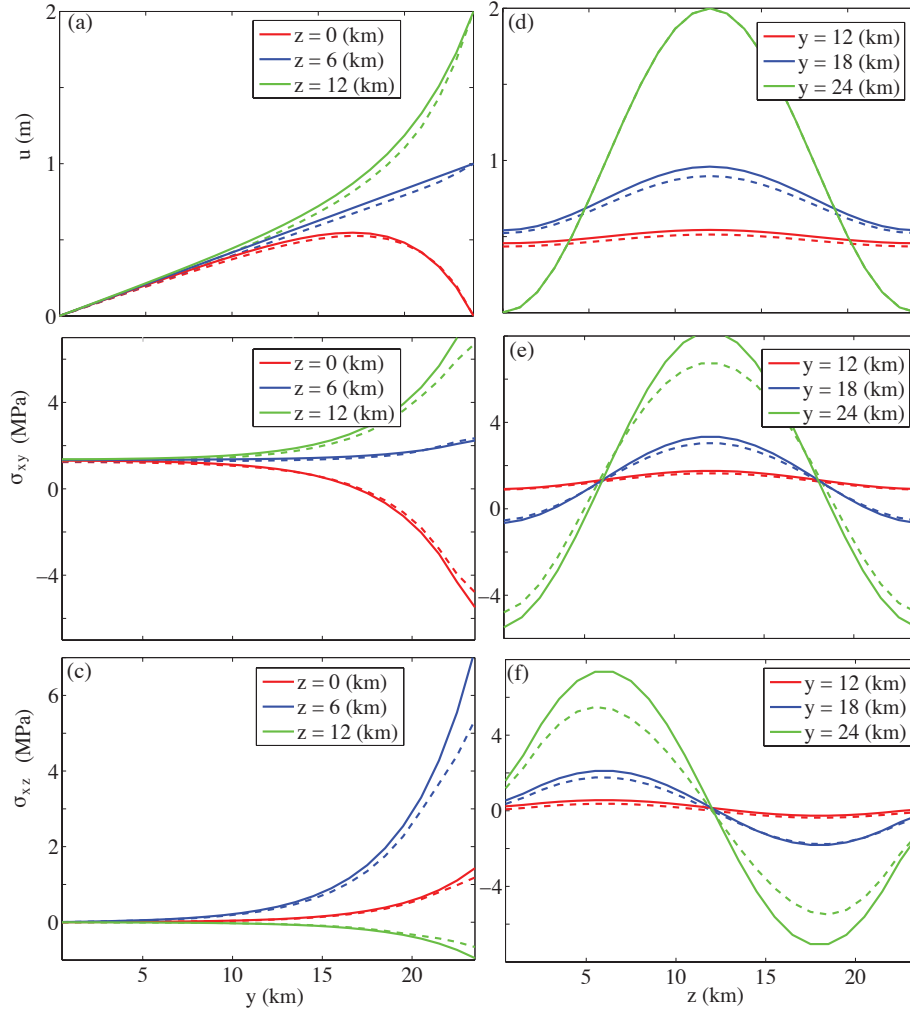


Figure 3: Contours of solution to (1) with boundary conditions (96) for elastic (solid lines) and plastic (dashed lines) material response. (a)-(b) displacement and (c)-(f) stress components. Plastic effects are seen most prominently in the stress contours which are reduced due to the yield condition.

748 found that for antiplane sliding between two anisotropic elastic materials,
 749 instability occurs for wave numbers below the critical wave number

750
$$k_{cr} = \frac{2(b-a)\sigma_n}{D_c \mu^*}, \quad (97)$$

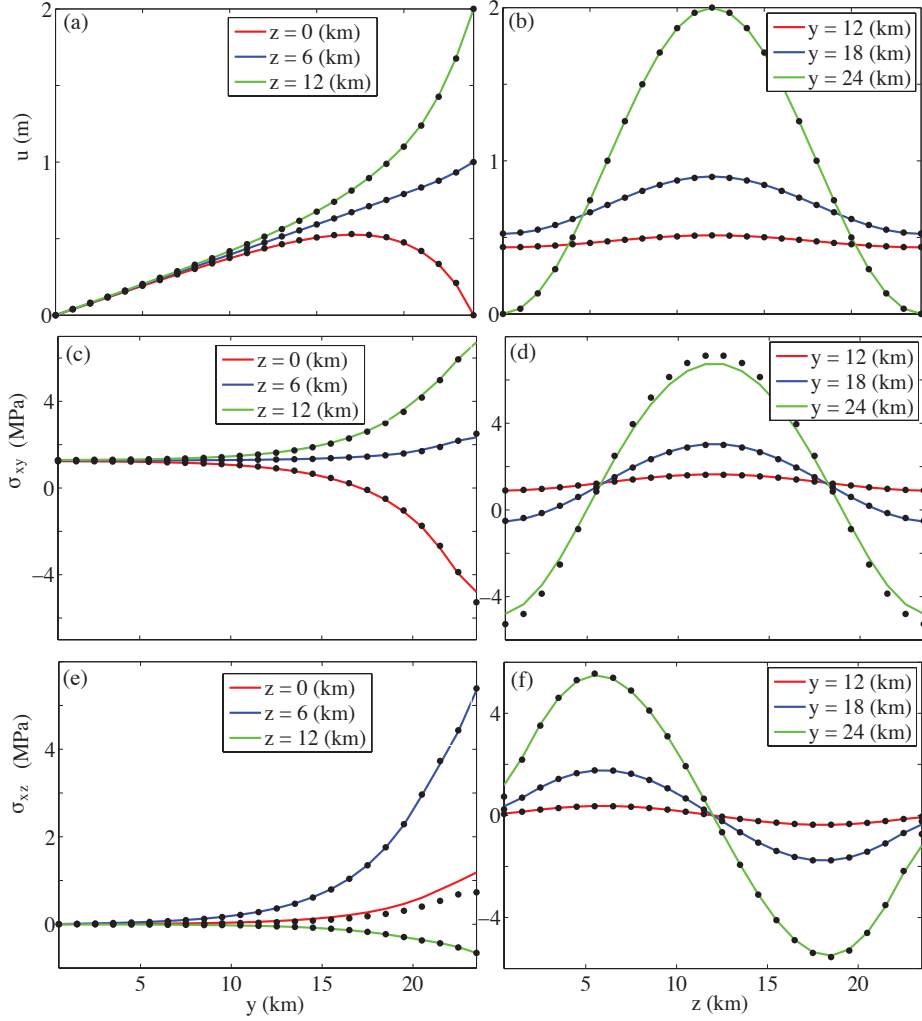


Figure 4: Contours of solution to (1) with boundary conditions (96) for plastic material response using the finite difference method (solid lines) and the finite element solution (black dots). (a)-(b) displacement and (c)-(f) stress components, with $N_y = N_z = 24$ points.

751 where

$$752 \quad \mu^* = \sqrt{\det(\bar{C}^{ep})}. \quad (98)$$

753 Thus the length scale

$$754 \quad h^* = \frac{2\pi}{k_{cr}} = \frac{\pi D_c \mu^*}{(b-a)\sigma_n} \quad (99)$$

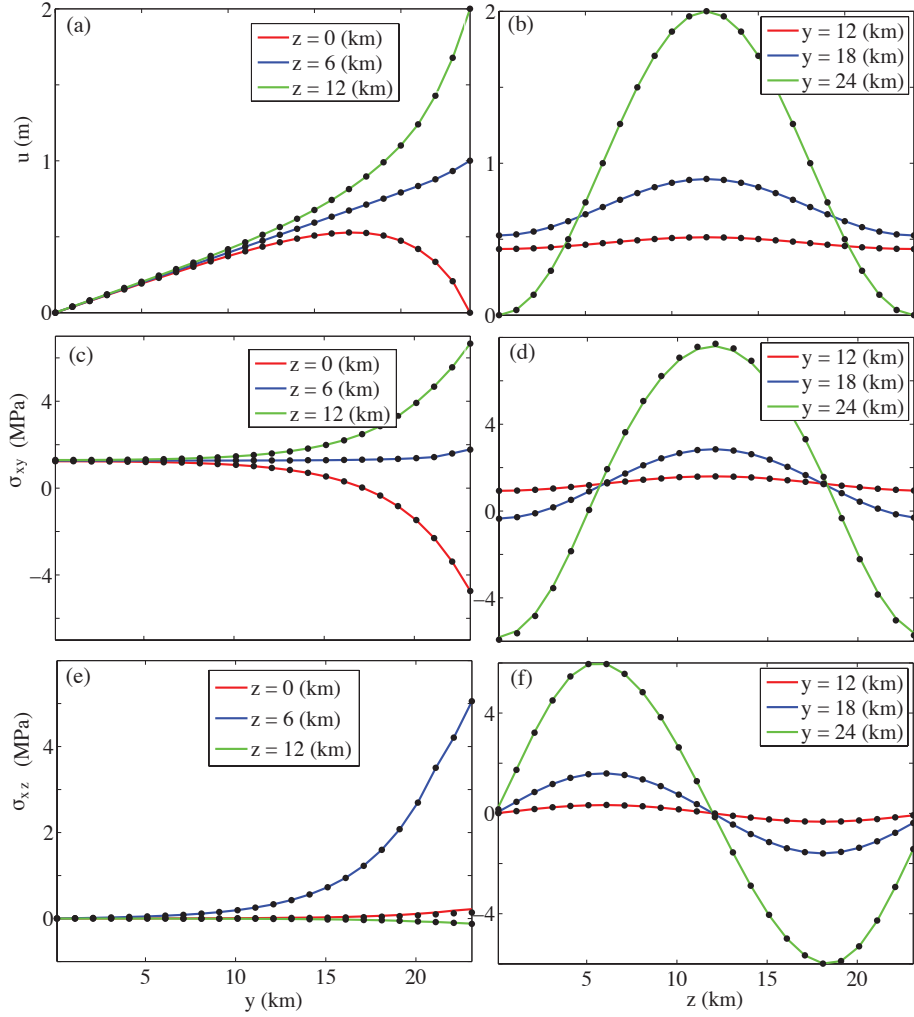


Figure 5: Contours of solution to (1) with boundary conditions (96) for plastic material response using the finite difference method (solid lines) and the finite element solution (black dots). (a)-(b) displacement and (c)-(f) stress components, with $N_y = N_z = 120$ points.

755 must be resolved by the grid to ensure accuracy of the solution.

756 As in *Erickson and Dunham (2014)*, we also need to resolve the region
 757 of rapid strength degradation immediately behind the tip of a propagating
 758 rupture, which is typically much smaller than h^* , and involves the rate-
 759 and-state parameters a and b in a different manner. By analogy to the

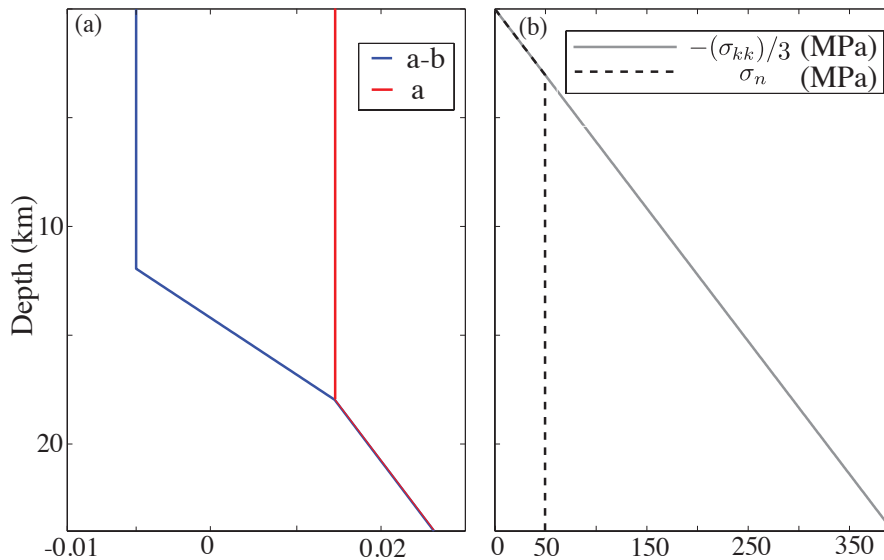


Figure 6: (a) Frictional parameters $a - b$ vary with depth. (b) Normal stress σ_n on fault vs. normal stresses in medium.

760 corresponding elastic problem (*Ampuero and Rubin, 2008*), we anticipate
 761 that this length scale will be approximately

$$762 \quad L_b = \frac{\mu^* D_c}{b \sigma_n}. \quad (100)$$

763 For all of our simulations, events nucleate near the transition zone from
 764 velocity weakening to velocity strengthening (at a depth of approximately 10
 765 km) and we chose values for parameters η and h primarily for computational
 766 (grid resolution) purposes. Since we use a variable grid spacing, we resolve
 767 h^* and L_b in our simulations with at least 60 and 5 grid points (respectively)
 768 near the free surface, with fewer (down to 12 and 1 grid point, respectively)
 769 at the nucleation depth, which we note seems less than desirable. To test that
 770 this grid spacing is adequate, however, we double the number of grid points
 771 for one scenario and the results appear qualitatively similar, see Appendix C.
 772 For the viscoplastic simulations we resolve the viscous relaxation time scale
 773 η/μ with at least 5 time steps.

774 For some parameter regimes, plastic yielding during the interseismic pe-
 775 riod is possible. For example, a decrease in cohesion c decreases the size of the
 776 elastic domain, so that plastic yielding can occur at lower stress states, see

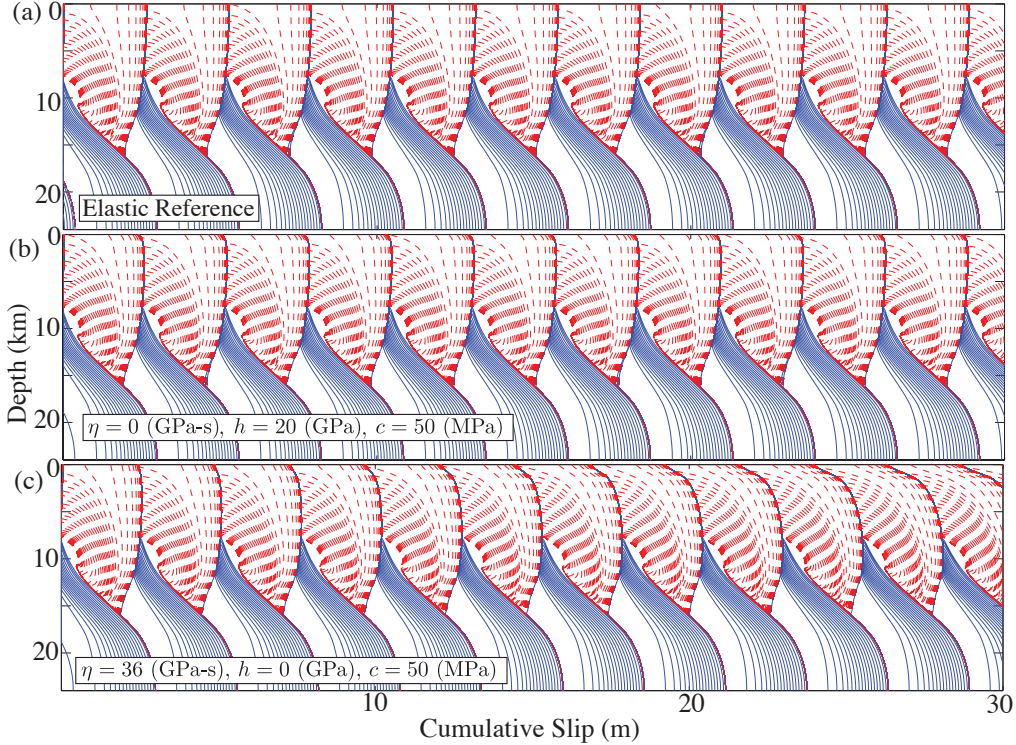


Figure 7: Snapshots of cumulative slip profiles plotted at 5-a intervals during interseismic period when $\max(V) \leq 1$ mm/s and dashed red profiles plotted at 1 s intervals during quasi-dynamic rupture for (a) elastic reference case, (b) $\eta = 0$ GPa-s, $h = 20$ GPa, $c = 50$ MPa, and (c) $\eta = 36$ GPa-s, $h = 0$ GPa, $c = 50$ MPa.

777 Figure 2. Although in reality plastic yielding may occur during all phases of
778 the earthquake cycle, we chose to explore scenarios where plastic response is
779 limited to the coseismic phase. This choice was made because viscoplasticity
780 introduces the time scale η/h which must be resolved by the time-stepping
781 method. For small values of η/h , the effective response during rupture is
782 plastic. Unfortunately, small η/h cannot be resolved during the interseis-
783 mic phase without taking unreasonably small time steps, thus we considered
784 large values of c such that plastic response occurs only at those stress levels
785 attained during rupture. The study of plastic yielding during all phases of
786 the earthquake cycle are deferred to future work.

787 Figures 7 and 8 show cumulative slip profiles plotted at 5-a intervals
788 during the interseismic period, which we define to be when $\max(V) \leq 1$

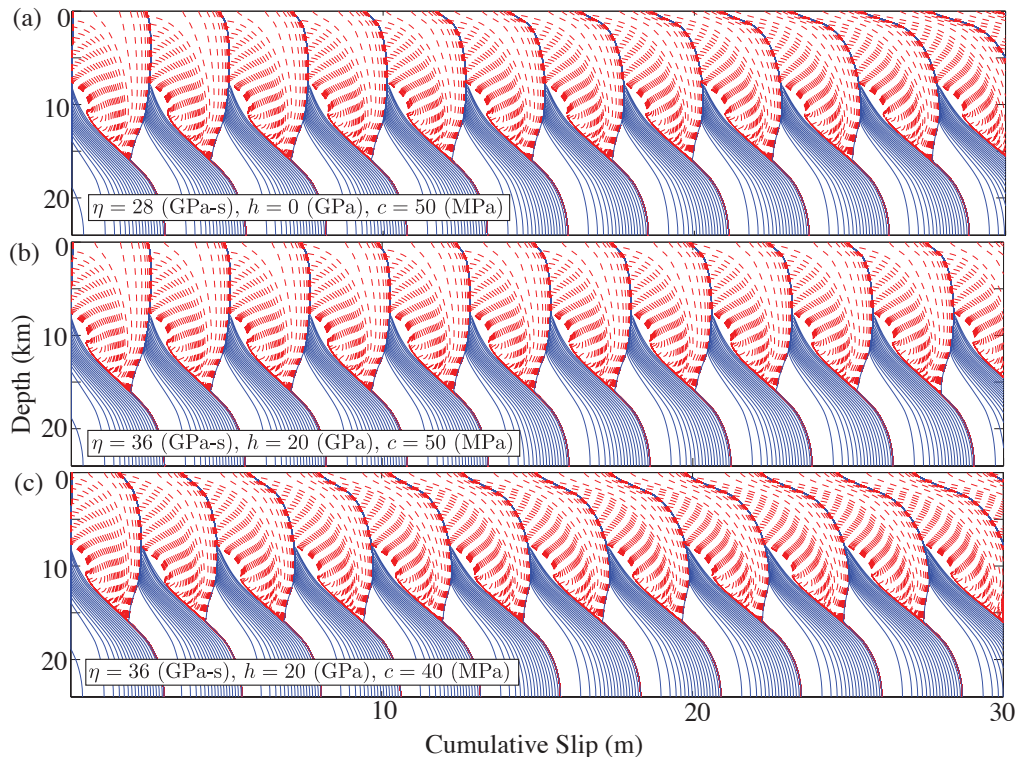


Figure 8: Snapshots of cumulative slip profiles plotted at 5-a intervals during interseismic period when $\max(V) \leq 1$ mm/s and dashed red profiles plotted at 1 s intervals during quasi-dynamic rupture for (a) $\eta = 28$ GPa-s, $h = 0$ GPa, $c = 50$ MPa, (b) $\eta = 36$ GPa-s, $h = 20$ GPa, $c = 50$ MPa, and (c) $\eta = 36$ GPa-s, $h = 20$ GPa, $c = 40$ MPa.

789 mm/s, and in dashed red contours every 1 s during quasi-dynamic rupture.
 790 Figure 7(a) is the elastic reference case used in *Erickson and Dunham (2014)*,
 791 where periodic cycles emerge. Slip below the velocity-weakening region creeps
 792 interseismically and approximately 3 m of slip occurs at the surface during
 793 each event. Note that during each event, the upper section of the fault
 794 catches up with slip at depth, characteristic of an elastic material response.
 795 For the plastic simulations, in all cases we found that after the first rupture,
 796 slip in the shallow surface is less than the slip at depth. The evolution of this
 797 slip deficit with each subsequent event is dictated by the plasticity model,
 798 however.

799 Figure 7(b) shows results from considering rate-independent plasticity
 800 with hardening parameter $h = 20$ GPa and cohesion $c = 50$ MPa. Plastic

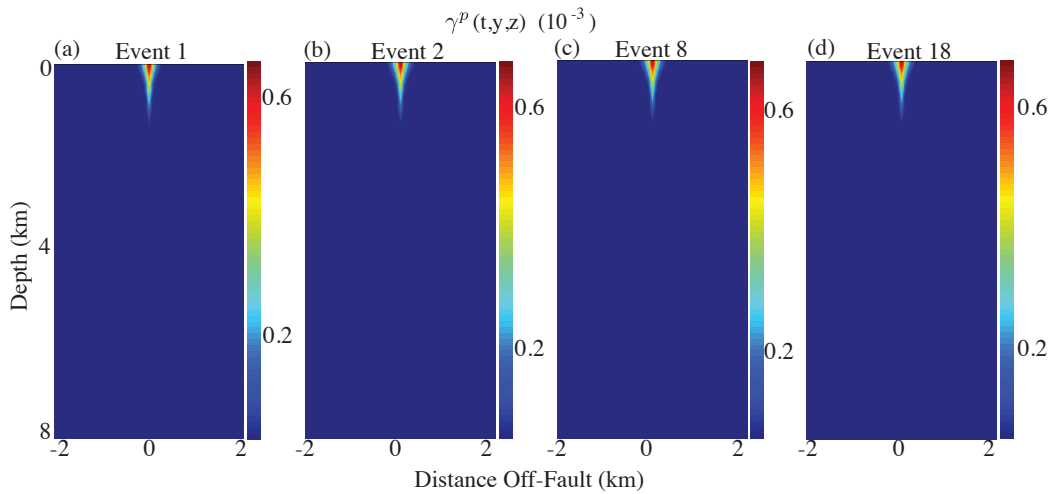


Figure 9: Off-fault equivalent plastic strain for $\eta = 0$ GPa-s, $h = 20$ GPa, $c = 50$ MPa after the first, second, eight and eighteenth rupture events. The magnitude and off-fault extent (~ 100 m during first rupture only) of plastic strain effectively saturates after the first event.

801 response occurs during the first event when the rupture reaches approxi-
 802 mately 3 km depth, but has only a slight influence on slip above this depth.
 803 During the first rupture, a small slip deficit emerges above ~ 1 km depth.
 804 Because hardening causes the yield surface to expand, the response during
 805 subsequent events is effectively elastic and the slip deficit remains largely un-
 806 changed. Figure 7(c) shows results from a viscoplastic simulation (without
 807 hardening) with $\eta = 36$ GPa-s and $c = 50$ MPa. The slip deficit in the upper
 808 3 km increases with subsequent ruptures, and after the tenth event, the slip
 809 deficit at the surface is approximately 2 m.

810 To assess the sensitivity to viscosity, we decrease η from 36 to 28 GPa-s,
 811 seen in Figure 8(a). The slip deficit in the upper 3 km also increases with
 812 subsequent rupture, and after the 10th event the slip deficit at the surface is
 813 approximately 3 m, suggesting that the slip deficit will increase at a faster
 814 rate for lower values of η for the viscoplastic model without hardening. Figure
 815 8(b) shows results from combined viscoplastic and hardening effects. For
 816 $\eta = 36$ GPa-s, $h = 20$ GPa and $c = 50$ MPa, the slip deficit increases with
 817 each rupture, but at a decreasing rate, and reaches a limiting value of ~ 1 m.

818 Decreasing the cohesion to 40 MPa, as shown in Figure 8(c), gener-
 819 ates a larger slip deficit (approximately 3.5 m at the surface after the 10th

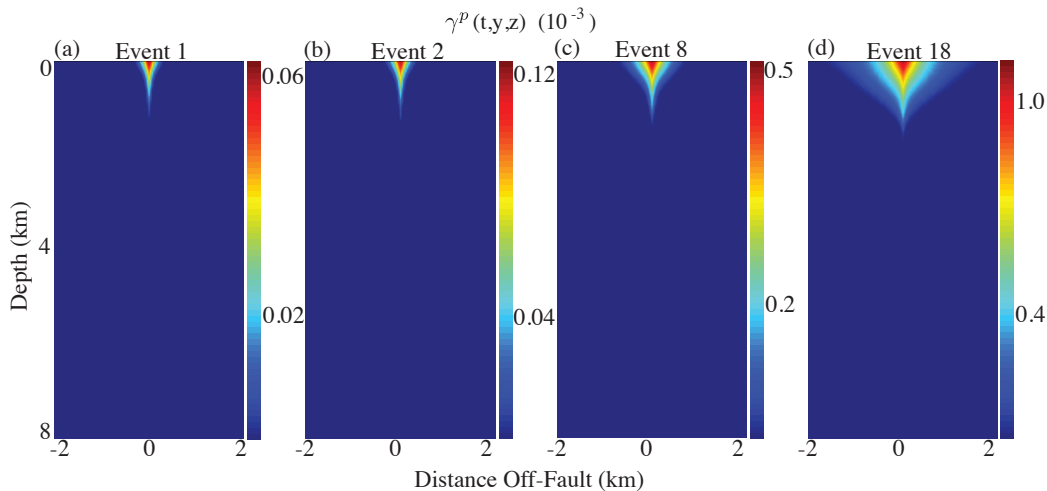


Figure 10: Off-fault equivalent plastic strain for $\eta = 36$ GPa-s, $h = 0$ GPa, $c = 50$ MPa after the first, second, eighth and eighteenth rupture events. The magnitude and off-fault extent (additional ~ 100 m per rupture) of plastic strain increases at an approximately constant rate with each rupture during the first 18 events.

820 event) than the analogous simulation in Figure 8(b), although with hardening
 821 present this deficit also saturates after several ruptures.

822 For the values we considered, cohesion determines the depth at which
 823 plastic response occurs during rupture (confined to about 1-2 km below
 824 Earth's surface). Figure 9 illustrates the evolution in off-fault equivalent
 825 plastic strain for the rate-independent simulation from Figure 7(a), during
 826 the first, second, eighth and eighteenth events. The first event generates
 827 plastic strain at depths above ~ 1 km and off the fault to about 200 m at the
 828 surface. The maximum value at the fault surface is approximately 0.7 mil-
 829 listrain and little increase in either extent or magnitude occurs after the first
 830 event. Figure 10 is the analogous figure for the viscoplastic model without
 831 hardening from Figure 7(b). The first event generates a maximum value of
 832 0.06 millistrain at the fault surface, extending out to approximately 300 m
 833 and to a depth of ~ 1 km. During all subsequent events the maximum value
 834 of plastic strain increases.

835 Adding hardening to the viscoplastic model decreases the magnitude and
 836 extent of additional plastic strain with each rupture, see Figure 11, so that
 837 by the eighteenth rupture, the distribution remains relatively unchanged by
 838 subsequent events. Figure 12 illustrates the effect of a decrease in cohesion

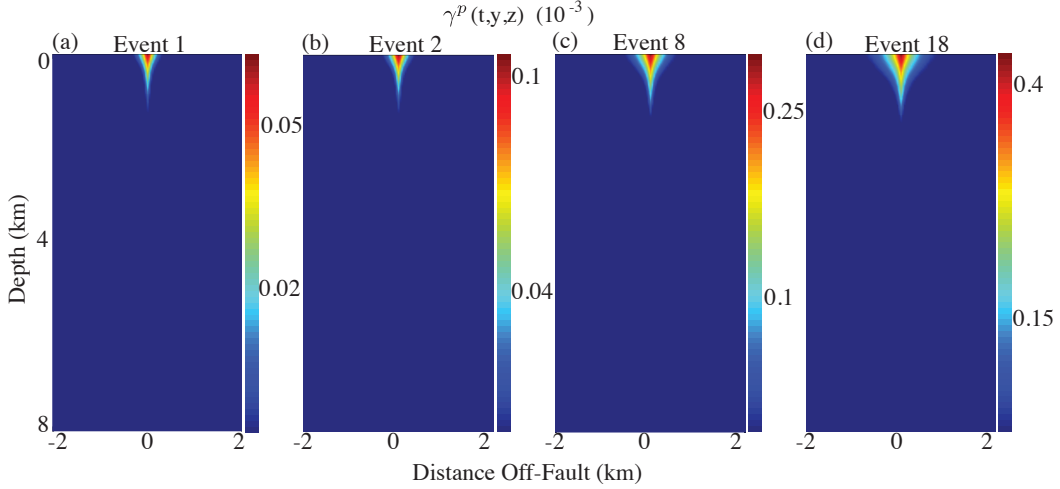


Figure 11: Off-fault equivalent plastic strain for $\eta = 36$ GPa-s, $h = 20$ GPa, $c = 50$ MPa after the first, second, eight and eighteenth rupture events. The magnitude and off-fault extent (~ 100 m during first rupture only) of plastic strain increases at an approximately decreasing rate with each rupture. After 18 events, the extent has saturated at < 1 km at the surface.

839 (from 50 to 40 MPa) which effectively lowers the yield stress so that plastic
 840 straining occurs at lower depths compared to previous simulations. Com-
 841 pared to the results shown in Figure 11, a decrease in cohesion increases the
 842 depth of plastic strain from 1 to 2 km during the first event. In addition, a
 843 decrease in cohesion generates more plastic strain and with greater extent.
 844 By the eighteenth event, plastic strain extends beyond 2 km at the surface.

845 The amount of tectonic offset accommodated by plastic strain, $u^p(t, z)$,
 846 can be computed by integrating the off-fault plastic strain, namely

$$847 \quad u^p(t, z) = 2 \int_0^{L_y} \gamma_{xy}^p(t, y, z) dy. \quad (101)$$

848 At the surface $z = 0$, the time history of u^p is plotted in Figure 13 and illus-
 849 trates how much tectonic offset is accommodated by inelastic deformation for
 850 different plasticity models. In particular, when rate-independent plasticity
 851 with hardening is used (cyan), the amount of offset due to inelastic deforma-
 852 tion is about 0.2 m after the first event and increases almost negligibly after
 853 the first event. If a viscoplastic relaxation is added (green), however, the
 854 amount of offset is lower during the first event, but increases with each rup-
 855 ture, reaching approximately 0.2 m after ~ 10 events. An increasing amount

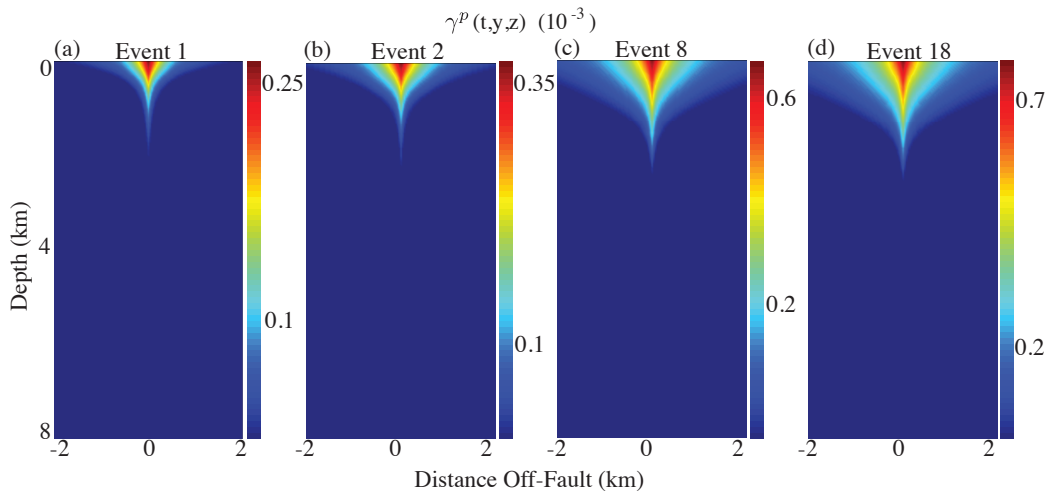


Figure 12: Off-fault equivalent plastic strain for $\eta = 36$ GPa-s, $h = 20$ GPa, $c = 40$ MPa after the first, second, eight and eighteenth rupture events. The magnitude and off-fault extent (~ 1 km during first rupture only) of plastic strain increases at an approximately decreasing rate with each rupture. After 18 events, the extent has begun to saturate near 2 km.

856 of offset accommodated by inelastic deformation occurs with each rupture
 857 for the viscoplastic models without hardening (black, blue, red), with lower
 858 values of viscosity generating greater amounts of inelastic deformation. For
 859 $\eta = 20$ GPa-s, for example, approximately 2 m of tectonic off-set is accom-
 860 modated by inelastic strain after ~ 10 events. The rate-independent simulation
 861 with hardening present (cyan) reveals that an upper limit to the amount of
 862 inelastic deformation exists, by virtue of the fact that hardening causes in
 863 expansion of the yield surface, as illustrated in Figure 2. The viscoplastic
 864 simulations with hardening (green and purple) show that inelastic yielding
 865 continues to occur (with greater overall amounts for lower values in cohesion),
 866 but at a decreasing rate, i.e for decreasing du^p/dt . Only the viscoplastic sim-
 867 ulations without hardening (black, blue, red) reveal that inelastic yielding
 868 continues to occur with an increasing amount of plastic strain accruing with
 869 each event ($du^p/dt \geq 0$).

870 10. Discussion

871 We have developed a finite difference method to account for off-fault
 872 plastic response over many quasi-dynamic ruptures. The computational

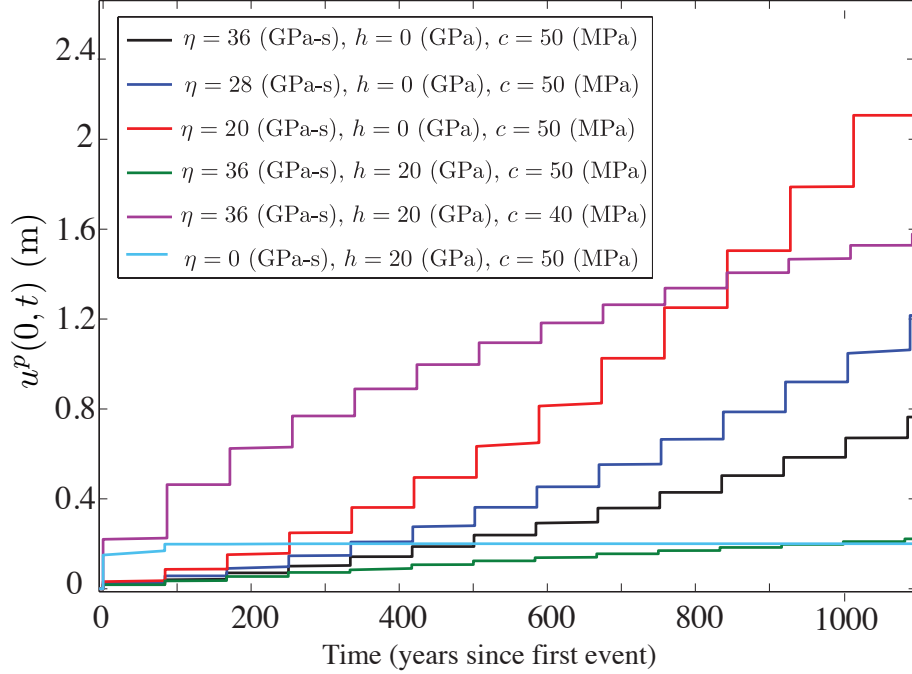


Figure 13: Time history of integrated plastic strain at the surface showing amount of tectonic offset accommodated by inelastic deformation.

873 framework can model both rate-independent plasticity and viscoplasticity, al-
 874 though we found that isotropic hardening is necessary in the rate-independent
 875 model for solveability of the underlying equations. We considered a Drucker-
 876 Prager model (which reduces to von-Mises plasticity in the antiplane scenario
 877 we considered) with a depth-dependent yield stress. Numerical results were
 878 verified through convergence tests and comparisons with the solution from a
 879 finite element software package. Future work includes a deeper exploration
 880 of parameter space. For example, the inclusion of a depth dependency of
 881 the internal friction angle and cohesion (like those derived in *Roten et al.*
 882 (2016)) will be considered. The effects of hardening and viscosity will fur-
 883 ther be explored, as our choices for these parameters were chosen primarily
 884 for efficiency of computation.

885 For the parameter study in this work, we found that viscosity, hardening,
 886 and cohesion all influence the extent and magnitude of off-fault plastic strain
 887 and all scenarios give rise to a shallow slip deficit. The inclusion of hard-

888 ening in all models sets an upper limit on the slip deficit, which is reached
 889 at a faster rate for lower values of viscosity. The viscoplastic models with
 890 no hardening, however, give rise to the largest slip deficits which increase
 891 continuously with subsequent rupture. Our results suggest that cumulative
 892 inelastic deformation over the course of many events can account for a sig-
 893 nificant amount of tectonic offset. We found that per rupture, ~ 0.1 m of
 894 integrated plastic strain accrues, corresponding to $\sim 10\%$ of the tectonic de-
 895 formation budget. Results from our model compare well to the observations
 896 of *Meade et al.* (2013) who estimate that $6\% \pm 9\%$ of deformation occurs off
 897 of several major strike-slip faults.

898 11. Acknowledgments

899 We thank the editor at JMPS for handling this manuscript, as well as
 900 four anonymous reviewers for helpful comments. This work was initiated
 901 while B.A.E. was supported by the NSF under Award No. EAR-0948304
 902 and completed with support from NSF under Award No. EAR-1547603 and
 903 by the Southern California Earthquake Center. SCEC is funded by NSF
 904 Cooperative Agreement EAR-0529922 and USGS Cooperative Agreement
 905 07HQAG0008 (SCEC contribution number 7166).

906 Appendix A. The Coordinate Transform and Penalty Parameters

907 As stated in section 6, we desire finer grid resolution in the domain near
 908 the fault and close to the free surface $z = 0$. Using coordinate transforms,
 909 we map the (y, z) grid in $[0, L_y] \times [0, L_z]$ with unequally spaced nodes, to a
 910 computational domain $(\xi_1, \xi_2) \in [0, 1] \times [0, 1]$ with equal grid spacings $(N_{\xi_1} + 1$
 911 and $N_{\xi_2} + 1$ grid points in each direction, with $\Delta\xi_1 = 1/N_{\xi_1}$, $\Delta\xi_2 = 1/N_{\xi_2}$).
 912 We let $N = (N_{\xi_1} + 1)(N_{\xi_2} + 1)$. The mapping is given by

$$913 \quad y = \ell_Y \tan(\tan^{-1}(L_y/\ell_Y)\xi_1) \quad (\text{A.1a})$$

$$914 \quad z = \ell_Z \tan(\tan^{-1}(L_z/\ell_Z)\xi_2). \quad (\text{A.1b})$$

915 Parameters $\ell_Y, \ell_Z > 0$ control the strength to which nodes are clustered
 916 near the fault and surface (respectively). The mapping (A.1) is invertible,
 917 with $\frac{\partial y}{\partial \xi_1}, \frac{\partial z}{\partial \xi_2} > 0$. The Jacobian J of the transformation is

$$918 \quad J = \begin{bmatrix} \frac{\partial y}{\partial \xi_1} & 0 \\ 0 & \frac{\partial z}{\partial \xi_2} \end{bmatrix} \quad (\text{A.2})$$

919 with determinant $|\mathbf{J}| = \frac{\partial \mathbf{y}}{\partial \xi_1} \otimes \frac{\partial \mathbf{z}}{\partial \xi_2}$ where $\frac{\partial \mathbf{y}}{\partial \xi_1}$ denotes the diagonal coefficient
 920 matrix, and $\frac{\partial \mathbf{y}}{\partial \xi_1}^{-1}$ is its inverse (reciprocals along the diagonal). Using the
 921 notation introduced in section 6, the SBP-SAT discretization of (33) on the
 922 computational domain is given by

$$\mathbf{0} = \mathbf{D}_{2\xi_1}^{\mathbf{a}_{11}} \mathbf{du} + \mathbf{D}_{\xi_1} \mathbf{a}_{12} \mathbf{D}_{\xi_2} \mathbf{du} + \mathbf{D}_{\xi_2} \mathbf{a}_{21} \mathbf{D}_y \mathbf{du} + \mathbf{D}_{2\xi_2}^{\mathbf{a}_{22}} \mathbf{du} + \tilde{\mathbf{P}}_L + \tilde{\mathbf{P}}_R + \tilde{\mathbf{P}}_T + \tilde{\mathbf{P}}_B, \quad (\text{A.3})$$

924 where the SAT penalty vectors enforcing boundary conditions (41) are

$$\tilde{\mathbf{P}}_L = \mathbf{H}_{\xi_1}^{-1} (\boldsymbol{\alpha}_L + \beta \mathbf{H}_{\xi_2}^{-1} (-\mathbf{a}_{11} \mathbf{S}_{\xi_1} - \mathbf{a}_{12} \mathbf{D}_{\xi_2})^T) \mathbf{H}_{\xi_2} \mathbf{E}_0 (\mathbf{du}_L - \mathbf{dg}_L) \quad (\text{A.4a})$$

$$\tilde{\mathbf{P}}_R = \mathbf{H}_{\xi_1}^{-1} (\boldsymbol{\alpha}_R + \beta \mathbf{H}_{\xi_2}^{-1} (\mathbf{a}_{11} \mathbf{S}_{\xi_1} + \mathbf{a}_{12} \mathbf{D}_{\xi_2})^T) \mathbf{H}_{\xi_2} \mathbf{E}_N (\mathbf{du}_R - \mathbf{dg}_R) \quad (\text{A.4b})$$

$$\tilde{\mathbf{P}}_T = -\mathbf{H}_{\xi_2}^{-1} (\mathbf{I}_{\xi_1} \otimes \mathbf{E}_0) ([-\mathbf{a}_{22} \mathbf{S}_{\xi_2} \mathbf{du} - \mathbf{a}_{21} \mathbf{D}_{\xi_1} \mathbf{du}]_T - \tilde{\mathbf{d}}\mathbf{g}_T) \quad (\text{A.4c})$$

$$\tilde{\mathbf{P}}_B = -\mathbf{H}_{\xi_2}^{-1} (\mathbf{I}_{\xi_1} \otimes \mathbf{E}_N) ([\mathbf{a}_{22} \mathbf{S}_{\xi_2} \mathbf{du} + \mathbf{a}_{21} \mathbf{D}_{\xi_1} \mathbf{du}]_B - \tilde{\mathbf{d}}\mathbf{g}_B) \quad (\text{A.4d})$$

929 where the modified boundary data are

$$\tilde{\mathbf{d}}\mathbf{g}_T = \frac{\partial \mathbf{y}}{\partial \xi_1} \mathbf{dg}_T \quad (\text{A.5a})$$

$$\tilde{\mathbf{d}}\mathbf{g}_B = \frac{\partial \mathbf{y}}{\partial \xi_1} \mathbf{dg}_B. \quad (\text{A.5b})$$

932 The modified diagonal coefficient matrices in (A.4) are

$$\mathbf{a}_{11} = \mathbf{C}_{11}^{ep} \left(\frac{\partial \mathbf{y}}{\partial \xi_1}^{-1} \otimes \frac{\partial \mathbf{z}}{\partial \xi_2} \right) \quad (\text{A.6a})$$

$$\mathbf{a}_{12} = \mathbf{C}_{12}^{ep} \quad (\text{A.6b})$$

$$\mathbf{a}_{21} = \mathbf{C}_{21}^{ep} \quad (\text{A.6c})$$

$$\mathbf{a}_{22} = \mathbf{C}_{22}^{ep} \left(\frac{\partial \mathbf{y}}{\partial \xi_1} \otimes \frac{\partial \mathbf{z}}{\partial \xi_2}^{-1} \right) \quad (\text{A.6d})$$

937 correspond to the moduli

$$a_{11} = C_{11}^{ep} \frac{\partial \xi_1}{\partial y} \quad (\text{A.7a})$$

$$a_{12} = C_{12}^{ep} \quad (\text{A.7b})$$

$$a_{21} = C_{21}^{ep} \quad (\text{A.7c})$$

$$a_{22} = C_{22}^{ep} \frac{\partial \xi_2}{\partial z} \quad (\text{A.7d})$$

942 of the transformed (continuous) problem, and we use the notation $a_{11i,j} =$
 943 $a_{11}(y_j, z_i)$ as in section 6. Letting

$$\bar{\mathbf{A}} = \begin{bmatrix} \mathbf{a}_{11} & \mathbf{a}_{12} \\ \mathbf{a}_{21} & \mathbf{a}_{22} \end{bmatrix}, \quad (\text{A.8})$$

symmetry of $\bar{\mathbf{A}}$ follows that of the 2×2 matrix \bar{C}^{ep} given by (34). That $\bar{\mathbf{A}}$ is positive-definite also follows from \bar{C}^{ep} : Express $\bar{\mathbf{A}}$ via the Schur decomposition $\bar{\mathbf{A}} = \mathbf{X}^T \mathbf{S} \mathbf{X}$, where

$$\mathbf{S} = \begin{bmatrix} \mathbf{a}_{11} & \mathbf{0} \\ \mathbf{0} & \mathbf{a}_{22} - \mathbf{a}_{21} \mathbf{a}_{11}^{-1} \mathbf{a}_{12} \end{bmatrix} \quad (\text{A.9})$$

and

$$\mathbf{X} = \begin{bmatrix} \mathbf{I} & \mathbf{a}_{11}^{-1} \mathbf{a}_{12} \\ \mathbf{0} & \mathbf{I} \end{bmatrix}. \quad (\text{A.10})$$

Since \mathbf{S} is a diagonal matrix, its eigenvalues lie along the diagonal. Positive-definiteness of \bar{C}^{ep} guarantees that each element along the diagonal of \mathbf{C}_{11}^{ep} is positive and the transformation (A.1) maintains that the diagonal matrix \mathbf{a}_{11} has positive elements. The diagonal matrix $\mathbf{a}_{22} - \mathbf{a}_{21} \mathbf{a}_{11}^{-1} \mathbf{a}_{12} = (\frac{\partial \mathbf{y}}{\partial \xi_1} \otimes \frac{\partial \mathbf{z}}{\partial \xi_2})^{-1} [\mathbf{C}_{11}^{ep}]^{-1} (\mathbf{C}_{11}^{ep} \mathbf{C}_{22}^{ep} - \mathbf{C}_{12}^{ep} \mathbf{C}_{21}^{ep})$ has positive elements by construction of the mapping and positive-definiteness of \bar{C}^{ep} . Thus positive-definiteness of $\bar{\mathbf{A}}$ follows from that of \mathbf{S} by the Sylvester Law of Inertia (*Golub and Van Loan*, 2013).

Applying the energy method to (A.3) and a proper choice of penalty parameters (given shortly) yields $\frac{d}{dt} \mathbf{dE} \leq 0$, where

$$\mathbf{dE} = \frac{1}{2} \mathbf{dU}^T (\mathbf{H}_{\xi_1} \otimes \mathbf{H}_{\xi_2}) \bar{\mathbf{A}} \mathbf{dU} + \frac{1}{2} \mathbf{du}^T (\mathbf{R}_{\xi_1}^{\mathbf{a}_{11}} \otimes \mathbf{H}_{\xi_2}) \mathbf{du} + \frac{1}{2} \mathbf{du}^T (\mathbf{H}_{\xi_1} \otimes \mathbf{R}_{\xi_2}^{\mathbf{a}_{22}}) \mathbf{du} + U_1 + U_2, \quad (\text{A.11})$$

where $\mathbf{dU} = [\mathbf{D}_{\xi_1} \mathbf{du} \ \mathbf{D}_{\xi_2} \mathbf{du}]^T$. U_1 and U_2 are non-negative quantities that arise from the weak enforcement of Dirichlet conditions, detailed shortly.

Note that uniform grid spacing, as considered in section 6, is the special case $\ell_Y, \ell_Z \rightarrow \infty$ and the transformation merely scales the overall size of the domain. In the case of uniform grid spacing, $\bar{\mathbf{A}} = \bar{C}^{ep}$. The stability results of section 6 are thus a special case of the results here.

The penalty parameters in (A.4) are derived in *Virta and Mattsson* (2014) and given here. The $N \times N$ diagonal coefficient matrix \mathbf{a}_{11} has j, k^{th} entry $\mathbf{a}_{11,j,k}$. *Virta and Mattsson* (2014) find that penalty parameter $\beta = -1$,

971 and penalty (diagonal) matrices $\boldsymbol{\alpha}_L$, $\boldsymbol{\alpha}_R$ have components obtained by first
 972 defining diagonal matrices \mathbf{b}_{1L} , \mathbf{b}_{1R} , \mathbf{b}_{2L} and \mathbf{b}_{2R} which have components

$$973 \quad b_{1L_{j,j}} = \beta_p(\Delta\xi_1)\lambda_{L_j}/(a_{11_{j,1}})^2 \quad (\text{A.12a})$$

$$974 \quad b_{1R_{j,j}} = \beta_p(\Delta\xi_1)\lambda_{R_j}/(a_{11_{j,N_{\xi_1}}})^2 \quad (\text{A.12b})$$

$$975 \quad b_{2L_{j,j}} = \delta_p(\Delta\xi_1)\lambda_{j,1}/(a_{22_{j,1}})^2 \quad (\text{A.12c})$$

$$976 \quad b_{2R_{j,j}} = \delta_p(\Delta\xi_1)\lambda_{j,N_{\xi_1}}/(a_{22_{j,N_{\xi_1}}})^2 \quad (\text{A.12d})$$

977 along the diagonal, where $\beta_p = 36/99$ and $\delta_p = 1/2$ (for the second order
 978 operators we consider),

$$979 \quad \lambda_{L_j} = \min(\lambda_{j,0}, \lambda_{j,1}), j = 0, \dots, N_{\xi_2} \quad (\text{A.13a})$$

$$980 \quad \lambda_{R_j} = \min(\lambda_{j,N_{\xi_1}-1}, \lambda_{j,N_{\xi_1}}), j = 0, \dots, N_{\xi_2}, \quad (\text{A.13b})$$

981 and

$$982 \quad \lambda_{j,k} = \frac{1}{2} \left(a_{11_{j,k}} + a_{22_{j,k}} - \sqrt{(a_{11_{j,k}} - a_{22_{j,k}})^2 + 4(a_{12_{j,k}})^2} \right). \quad (\text{A.14a})$$

983 The positive quantities given in the incremental internal energy are

$$984 \quad U_1 = \mathbf{U}_L^T \mathbf{H}_3 \mathbf{T}_L \mathbf{U}_L \quad (\text{A.15a})$$

$$985 \quad U_2 = \mathbf{U}_R^T \mathbf{H}_3 \mathbf{T}_R \mathbf{U}_R \quad (\text{A.15b})$$

986 for vectors

$$987 \quad \mathbf{U}_L = [\mathbf{d}\mathbf{u}_L^T \quad (\mathbf{B}^{\mathbf{a}_{11}} \mathbf{S}_{\xi_1} \mathbf{d}\mathbf{u})_L^T \quad (\mathbf{a}_{12} \mathbf{D}_{\xi_1} \mathbf{d}\mathbf{u})_L^T]^T, \quad (\text{A.16a})$$

$$988 \quad \mathbf{U}_R = [\mathbf{d}\mathbf{u}_R^T \quad (\mathbf{B}^{\mathbf{a}_{11}} \mathbf{S}_{\xi_1} \mathbf{d}\mathbf{u})_R^T \quad (\mathbf{a}_{12} \mathbf{D}_{\xi_1} \mathbf{d}\mathbf{u})_R^T]^T, \quad (\text{A.16b})$$

$$989 \quad \mathbf{H}_3 = \text{diag}([\mathbf{H}_{\xi_1} \otimes \mathbf{H}_{\xi_2}, \quad \mathbf{H}_{\xi_1} \otimes \mathbf{H}_{\xi_2}, \quad \mathbf{H}_{\xi_1} \otimes \mathbf{H}_{\xi_2}]). \quad (\text{A.16c})$$

990 Matrix $\mathbf{B}^{\mathbf{a}_{11}}$ is a coefficient matrix for \mathbf{a}_{11} formed in a special way (see *Virta*
 991 *and Mattsson* (2014) for details). Matrices

$$992 \quad \mathbf{T}_L = \begin{bmatrix} -\boldsymbol{\alpha}_L & -\mathbf{1} & -\mathbf{1} \\ -\mathbf{1} & \mathbf{b}_{1R} & \mathbf{0} \\ -\mathbf{1} & \mathbf{0} & \mathbf{b}_{2R} \end{bmatrix} \quad (\text{A.17a})$$

993 and

$$994 \quad \mathbf{T}_R = \begin{bmatrix} -\boldsymbol{\alpha}_R & -\mathbf{1} & -\mathbf{1} \\ -\mathbf{1} & \mathbf{b}_{1L} & \mathbf{0} \\ -\mathbf{1} & \mathbf{0} & \mathbf{b}_{2L} \end{bmatrix} \quad (\text{A.18a})$$

995 are shown to be positive semi-definite if

$$996 \quad \alpha_{L_{j,j}} \leq -\frac{1}{b_{1R_{j,j}}} - \frac{1}{b_{2R_{j,j}}}, \quad j = 0, \dots, N_{\xi_2} \quad (\text{A.19a})$$

$$997 \quad \alpha_{R_{j,j}} \leq -\frac{1}{b_{1R_{j,j}}} - \frac{1}{b_{2R_{j,j}}}, \quad j = 0, \dots, N_{\xi_2} \quad (\text{A.19b})$$

998 (*Virta and Mattsson, 2014*).

999 Appendix B. The Consistent Tangent Moduli

1000 The consistent tangent moduli for both rate-independent and viscoplas-
1001 ticity are derived here simultaneously. Applying a backward-Euler discretiza-
1002 tion to the flow rule (19), we have

$$1003 \quad \sigma_{ij}^{n+1} = C_{ijkl}(\epsilon_{kl}^{n+1} - \epsilon_{kl}^{p,n+1}) = C_{ijkl}(\epsilon_{kl}^{n+1} - \epsilon_{kl}^{p,n} - d\lambda^{n+1} \frac{s_{kl}^{n+1}}{2\bar{\tau}^{n+1}}). \quad (\text{B.1})$$

1004 The consistent elastoplastic tangent stiffness tensor $\mathcal{C}_{ijkl}^{ep,n+1} = \frac{\partial \sigma_{ij}^{n+1}}{\partial \epsilon_{kl}^{n+1}}$ can be
1005 computed by first defining a few terms. Following *Simo and Hughes (1998)*,
1006 let $n_{ij} = s_{ij}/2\bar{\tau}$. Then

$$1007 \quad \frac{\partial n_{ij}}{\partial s_{kl}} = \frac{1}{\bar{\tau}} \left[\frac{1}{2} I_{ijkl} - n_{ij} n_{kl} \right], \quad (\text{B.2})$$

1008 where the fourth order, symmetric identity tensor

$$1009 \quad I_{ijkl} = \frac{1}{2} [\delta_{ik} \delta_{jl} + \delta_{il} \delta_{jk}]. \quad (\text{B.3})$$

1010 It is a quick exercise to show that

$$1011 \quad n_{ij}^{*,n+1} = n_{ij}^{n+1}, \quad (\text{B.4})$$

1012 and therefore we have

$$1013 \quad \frac{\partial \bar{\tau}^{*,n+1}}{\partial \epsilon_{kl}^{n+1}} = \frac{1}{\bar{\tau}^{*,n+1}} \sigma_{kl}^{*,n+1} \mu = 2\mu n_{kl}^{*,n+1} = 2\mu n_{kl}^{n+1}. \quad (\text{B.5})$$

1014 Next, recall the plastic consistency condition (71), which can be expressed

$$1015 \quad \bar{\tau}^{*,n+1} - \sigma_Y - h\gamma_p^n = (\eta/dt + \mu + h)d\lambda^{n+1} \quad (\text{B.6})$$

1016 where the rate-independent case is obtained by taking $\eta = 0$. Taking the
 1017 partial derivative of (B.6) yields

$$1018 \quad \frac{\partial \bar{\tau}^{*,n+1}}{\partial \epsilon_{kl}^{n+1}} = (\eta/dt + \mu + h) \frac{\partial d\lambda^{n+1}}{\partial \epsilon_{kl}^{n+1}}. \quad (\text{B.7})$$

1019 Re-arranging (B.7) and substituting in (B.5) yields

$$1020 \quad \frac{\partial \Delta\lambda^{n+1}}{\partial \epsilon_{kl}^{n+1}} = \frac{2\mu}{\eta/dt + \mu + h} n_{kl}^{n+1}. \quad (\text{B.8})$$

1021 Also note that we have,

$$1022 \quad C_{ijmn} \frac{\partial s_{mn}}{\partial \epsilon_{kl}} = 2\mu \frac{\partial s_{ij}}{\partial \epsilon_{kl}}. \quad (\text{B.9})$$

1023 Therefore

$$1024 \quad \frac{\partial n_{ij}^{n+1}}{\partial \epsilon_{kl}^{n+1}} = \frac{\partial n_{ij}^{*,n+1}}{\partial \epsilon_{kl}^{n+1}} = \frac{\partial n_{ij}^{*,n+1}}{\partial \sigma_{mn}^{*,n+1}} \frac{\partial \sigma_{mn}^{*,n+1}}{\partial \epsilon_{kl}^{n+1}} = \frac{\partial n_{ij}^{*,n+1}}{\partial \sigma_{mn}^{*,n+1}} C_{mnkl} = 2\mu \frac{\partial n_{ij}^{*,n+1}}{\partial \sigma_{kl}^{*,n+1}} = 2\mu \frac{\partial n_{ij}^{n+1}}{\partial s_{kl}^{n+1}}. \quad (\text{B.10})$$

1025 When plastic straining is occurring (i.e. when $\lambda > 0$), we can compute the
 1026 consistent elastoplastic tangent stiffness tensor by taking the partial deriva-
 1027 tive of equation (B.1)

$$1028 \quad \mathcal{C}_{ijkl}^{ep,n+1} = \frac{\partial \sigma_{ij}^{n+1}}{\partial \epsilon_{ij}^{n+1}} = C_{ijkl} - \frac{\partial d\lambda^{n+1}}{\partial \epsilon_{kl}^{n+1}} \mu n_{ij}^{n+1} - d\lambda^{n+1} \mu \frac{\partial n_{ij}^{n+1}}{\partial \epsilon_{kl}^{n+1}} \quad (\text{B.11})$$

$$1029 \quad = C_{ijkl} - \frac{2\mu}{\eta/dt + \mu + h} n_{kl}^{n+1} 2\mu n_{ij}^{n+1} - d\lambda^{n+1} 2\mu \left(2\mu \frac{\partial n_{ij}^{n+1}}{\partial s_{kl}^{n+1}} \right) \quad (\text{B.12})$$

$$1030 \quad = C_{ijkl} - \frac{4\mu^2}{\eta/dt + \mu + h} n_{kl}^{n+1} n_{ij}^{n+1} - d\lambda^{n+1} 4\mu^2 \frac{1}{\bar{\tau}^{n+1}} \left[\frac{1}{2} I_{ijkl} - n_{ij}^{n+1} n_{kl}^{n+1} \right] \quad (\text{B.13})$$

1031 and the specific case for antiplane motion given in (73)-(75) for rate-independent
 1032 plasticity, and (78)-(80) for viscoplasticity follow, using the notation $\mathcal{C}_{11}^{ep} =$
 1033 \mathcal{C}_{xyxy}^{ep} , $\mathcal{C}_{22}^{ep} = \mathcal{C}_{xzxz}^{ep}$, $\mathcal{C}_{12}^{ep} = \mathcal{C}_{xyxz}^{ep}$, $\mathcal{C}_{21}^{ep} = \mathcal{C}_{xzxxy}^{ep}$.

1034 Appendix C. Mesh Refinement

1035 We double the number of grid points used in the simulation shown in
 1036 Figure 7(c) with $\eta = 36$, $h = 0$ and $c = 50$ MPa, see Fig. C.14. Although a
 1037 bit more slip occurs with each rupture when mesh refining (note last event
 1038 for each simulation, for example), the results appear qualitatively similar.

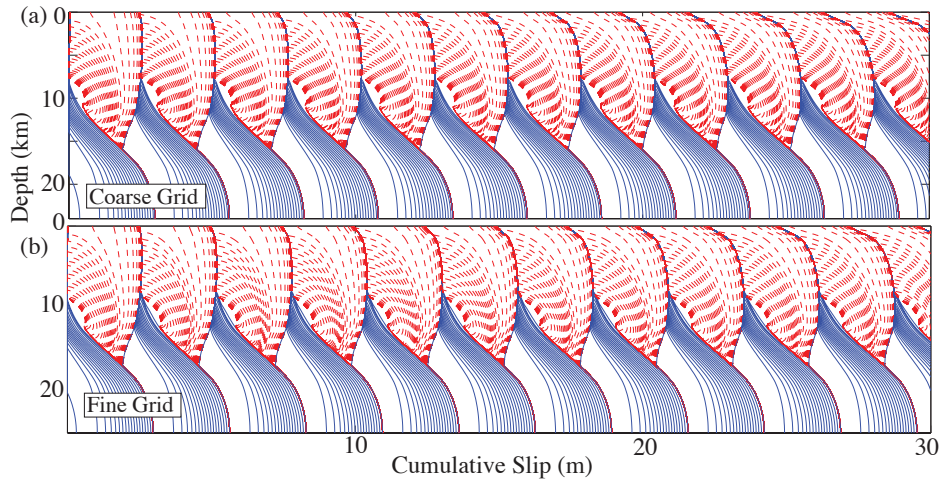


Figure C.14: Snapshots of cumulative slip profiles plotted at 5-s intervals during interseismic period when $\max(V) \leq 1$ mm/s and dashed red profiles plotted at 1 s intervals during quasi-dynamic rupture for $\eta = 36$ GPa-s, $h = 0$ GPa, $c = 50$ MPa for (a) the coarse grid simulation from Fig. 7(c) (plotted again for ease of comparison) and (b) results when using twice the number of grid points.

- 1039 Aagaard, B. T., Knepley, M. G. and Williams, C. A. (2013), A domain
 1040 decomposition approach to implementing fault slip in finite-element models
 1041 of quasi-static and dynamic crustal deformation, *J. Geophys. Res.*, **118**,
 1042 3059–3079, doi:10.1002/jgrb.50217
- 1043 Allison, K. L. and Dunham, E. M. (2016), Earthquake cycle simulations with
 1044 rate-and-state friction and nonlinear Maxwell rheology. *Tectonophysics*,
 1045 submitted.
- 1046 Ampuero, J.-P. and Rubin, A. M. (2008), Earthquake nucleation on rate
 1047 and state faults: Aging and slip laws, *J. Geophys. Res.*, **113**, B01302, doi:
 1048 10.1029/2007JB005082.
- 1049 Barbot, S., Lapusta, N. and Avouac, J.-P. (2012), Under the hood of the
 1050 earthquake machine: Toward predictive modeling of the seismic cycle, *Sci-*
 1051 *ence*, **336**, 707–710, doi:10.1126/science.1218796.
- 1052 Ben-Zion, Y. and Sammis, C. (2011), Brittle Deformation of Solid and Gran-
 1053 ular Materials with Applications to Mechanics of Earthquakes and Faults,
 1054 *Pure Appl. Geophys.*, **168**, 2147–2149, doi:10.1007/s00024-011-0418-8.

- 1055 Bower, A. F. (2010), Applied Mechanics of Solids, Taylor and Francis Group,
1056 LLC, CRC Press, Boca Raton, FL.
- 1057 Chen, W. F. and Han, D. J. (1988), *Plasticity for Structural Engineers*, first
1058 ed., Springer-Verlag, New York, 1–606.
- 1059 Chester, F. M., Evans, J. P. and Biegel, R. L. (1993), Internal structure
1060 and weakening mechanisms of the San Andreas fault, *J. Geophys. Res.*, **98**,
1061 771–786, doi:10.1029/92JB01866.
- 1062 Chester, F. M. and Logan, J. M. (1986), Implications for mechanical prop-
1063 erties of brittle faults from observations of the Punchbowl fault zone, Cal-
1064 ifornia, *Pure Appl. Geophys.*, **124**, 79–106 doi:10.1007/BF00875720.
- 1065 de Souza Neto, E. A., Perić, D. and Owen, D. R. J. (2008), *Computational*
1066 *Methods for Plasticity*, first ed., John Wiley & Sons Ltd, United Kingdom,
1067 1–791. DeSouza
- 1068 Dieterich, J. H. (1979), Modeling of rock friction: 1. Experimental results
1069 and constitutive equations, *J. Geophys. Res.*, **84**, 2161–2168, doi:10.1029/
1070 JB084iB05p02161.
- 1071 Drucker, D. C. (1959), A definition of a stable inelastic material, *J. Appl.*
1072 *Mech. ASME*, **26**, 101–195.
- 1073 Dunham, E. M., Belanger, D., Cong, L. and Kozdon, J. E. (2011a), Earth-
1074 quake ruptures with strongly rate-weakening friction and off-fault plastic-
1075 ity, Part 1: Planar faults, *Bull. Seismol. Soc. Am.*, **101**, 5, 2296–2307,
1076 doi:10.1785/0120100075.
- 1077 Dunham, E. M., Belanger, D., Cong, L. and Kozdon, J. E. (2011b), Earth-
1078 quake ruptures with strongly rate-weakening friction and off-fault plastic-
1079 ity, Part 2: Nonplanar faults, *Bull. Seismol. Soc. Am.*, **101**, 5, 2308–2322,
1080 doi:10.1785/0120100076.
- 1081 Dunne, F. and Petrinic, N. (2006), *Introduction to Computational Plasticity*,
1082 first ed., Oxford University Press, New York, 1–242.
- 1083 Duru, K. and Virta, K. (2014), Stable and high order accurate difference
1084 methods for the elastic wave equation in discontinuous media, *J. Comp.*
1085 *Phys.*, **279**, 37–62, doi:10.1016/j.jcp.2014.08.046.

- 1086 Erickson, B. A., and Dunham, E. M. (2014), An efficient numerical method
 1087 for earthquake cycles in heterogeneous media: Alternating subbasin and
 1088 surface-rupturing events on faults crossing a sedimentary basin, *J. Geophys.*
 1089 *Res.*, **119**, 1–27, doi:10.1002/2013JB010614.
- 1090 Faulkner, D. R., Jackson, C. A. L., Lunn, R. J. , Schlische, R. W., Shipton, Z.
 1091 K. , Wibberley, C. A. J. and Withjack, M. O. (2010), A review of recent
 1092 developments concerning the structure, mechanics and fluid flow properties
 1093 of fault zones, *J. Struct. Geol.*, **32**, 11, 1557–1575, doi:10.1016/j.jsg.2010.
 1094 06.009.
- 1095 Gabriel, A.-A., Ampuero, J.-P., Dalguer, L. A. and Mai, P. M. (2013), Source
 1096 properties of dynamic rupture pulses with off-fault plasticity, *J. Geophys.*
 1097 *Res.*, **118**, 8, 4117–4126, doi:10.1002/jgrb.50213.
- 1098 Gabriel, A.-A., Ampuero, J.-P., Dalguer, L. A. and Mai, P. M. (2013),
 1099 The transition of dynamic rupture styles in elastic media under
 1100 velocity-weakening friction, *J. Geophys. Res.*, **117**, B09311, doi:10.1029/
 1101 2012JB009468.
- 1102 Glowinski, R., and Le Tallec, P. (1989), Augmented Lagrangian and Opera-
 1103 tor Splitting Methods in Nonlinear Mechanics, Society for Industrial and
 1104 Applied Mathematics, Philadelphia, Volume 9.
- 1105 Golub, G. H. and Van Loan, C. F. (2013), Matrix Computations, 4th edition,
 1106 JHU press, Baltimore.
- 1107 Gustafsson, B. (2008), High Order Difference Methods for Time Dependent
 1108 PDE, Springer-Verlag, Berlin, doi:10.1007/978-3-540-74993-6.
- 1109 Horn, R. A. and Johnson, C. R. (1985), Matrix Analysis, Cambridge Univer-
 1110 sity Press, New York.
- 1111 Jain, S. K. (2008), Introduction to Theories of Plasticity, Part 1: Stress-
 1112 Strain Relations, Engineering Publications, Virginia.
- 1113 Johnson, K. M. and Segall, P. (2004), Viscoelastic earthquake cycle mod-
 1114 els with deep stress-driven creep along the SanAndreas fault system, *J.*
 1115 *Geophys. Res.*, **109**, B10403, doi:10.1029/2004JB003096.

- 1116 Kaneko, Y., Ampuero, J.-P. and Lapusta, N. (2011), Spectral-element simu-
1117 lations of long-term fault slip: Effect of low-rigidity layers on earthquake-
1118 cycle dynamics, *J. Geophys. Res.*, **116**, B10313, 1–18, doi:10.1029/
1119 2011JB008395.
- 1120 Kaneko, Y., and Fialko, Y. (2011), Shallow slip deficit due to large strike-slip
1121 earthquakes in dynamic rupture simulations with elasto-plastic off-fault
1122 response, *Geophys. J. Int.*, **186**, 1389–1403, doi:10.1111/j.1365-246X.2011.
1123 05117.x.
- 1124 Kozdon, J. E., Dunham, E. M. and Nordström, J. (2012), Interaction of waves
1125 with frictional interfaces using summation-by-parts difference operators:
1126 Weak enforcement of nonlinear boundary conditions, *J. Sci. Comput.*, **50**,
1127 341–367, doi:10.1007/s10915-011-9485-3.
- 1128 Kreiss, H.-O. and Scherer, G. (1974), Finite element and finite difference
1129 methods for hyperbolic partial differential equations, *Mathematical aspects*
1130 *of finite elements in partial differential equations*, Academic Press, Inc.,
1131 195–212, doi:10.1016/B978-0-12-208350-1.50012-1.
- 1132 Kreiss, H.-O. and Scherer, G. (1977), On the existence of energy estimates for
1133 difference approximations for hyperbolic systems, *Technical Report*, Dept.
1134 of Scientific Computing, Uppsala University.
- 1135 Lapusta, N., Rice, J. R., Ben-Zion, Y. and Zheng, G. (2000), Elastodynamic
1136 analysis for slow tectonic loading with spontaneous rupture episodes on
1137 faults with rate-and-state dependent friction, *J. Geophys. Res.*, **105**, 23765–
1138 23789, doi:10.1029/2000JB900250.
- 1139 Ma, S. and Andrews, D. J. (2010), Inelastic off-fault response and three-
1140 dimensional earthquake rupture dynamics on a strike-slip fault, *J. Geo-
1141 phys. Res.*, **115**, B04304, doi:10.1029/2009JB006382.
- 1142 Marone, C. (1998), Laboratory-derived friction laws and their application to
1143 seismic faulting, *Annu. Rev. Earth Planet. Sci.*, **26**, 643–696, doi:10.1146/
1144 annurev.earth.26.1.643.
- 1145 Mattsson, K. (2011), Summation by parts operators for finite difference ap-
1146 proximations of second-derivatives with variable coefficients, *J. Sci. Com-
1147 put.*, **51**, 650–682, doi:10.1007/s10915-011-9525-z.

- 1148 Mattsson, K. and Nordström, J. (2004), Summation by parts operators for
1149 finite difference approximations of second derivatives, *J. Comput. Phys.*,
1150 **199**, 503–540, doi:10.1016/j.jcp.2004.03.001.
- 1151 Mattsson, K., Ham, F. and Iaccarino, G. (2008), Stable and accurate wave-
1152 propagation in discontinuous media, *J. Comput. Phys.*, **227**, 8753–8767
1153 doi:10.1016/j.jcp.2004.03.001.
- 1154 Mazzoni, S., McKenna, F., Scott, M. H., and Fenves, G. L., (2009), Open
1155 system for earthquake engineering simulation user manual. University of
1156 California, Berkeley.
- 1157 Meade, B. J., Klinger, Y., and Hetland, E. A., (2013), Inference of multiple
1158 earthquake-cycle relaxation timescales from irregular geodetic sampling of
1159 interseismic deformation, *Bull. Seismol. Soc. Am.*, **103**, 2824–2835 doi:
1160 10.1785/0120130006.
- 1161 Mitchell, T. M. and Faulkner, D. R. (2009), The nature and origin of off-fault
1162 damage surrounding strike-slip fault zones with a wide range of displace-
1163 ments: A field study from the Atacama fault zone, northern Chile, *J.*
1164 *Struct. Geol.*, **31**, 8, 802–816, doi:10.1016/j.jsg.2009.05.002.
- 1165 Nordström, J., Mattsson, K. and Swanson, C. (2007), Boundary conditions
1166 for a divergence free velocity-pressure formulation of the Navier-Stokes
1167 equations, *J. Comput. Phys.*, **225**, 874–890, doi:10.1016/j.jcp.2007.01.010.
- 1168 Perzyna, P. (1966), Fundamental Problems in Viscoplasticity, *Advances*
1169 *in Applied Mechanics*, **9**, 243 - 377, doi:http://dx.doi.org/10.1016/
1170 S0065-2156(08)70009-7.
- 1171 Perzyna, P. (1971), Thermodynamic Theory of Viscoplasticity, *Advances*
1172 *in Applied Mechanics*, **11**, 313 - 354, doi:http://dx.doi.org/10.1016/
1173 S0065-2156(08)70345-4.
- 1174 Power, W. L and Tullis, T. E. (1991), Euclidean and fractal models for the
1175 description of rock surface roughness, *J. Geophys. Res.*, **96**, B1, 415–424,
1176 doi:10.1029/90JB02107.
- 1177 Ranjith, K. (2008), Dynamic anti-plane sliding of dissimilar anisotropic
1178 linear elastic solids, *Int. J. Solids Struct.*, **45**, 4211–4221, doi:10.1016/j.
1179 ijsolstr.2008.03.002.

- 1180 Rice, J. R. (1992), Fault stress states, pore pressure distributions and the
1181 weakness of the San Andreas fault, in *Fault Mechanics and Transport Prop-*
1182 *erties of Rock*, edited by Evans, B. and Wong, T.-F., 475 – 503, Academic,
1183 San Diego, Calif.
- 1184 Rice, J. R. (1993), Spatio-temporal complexity of slip on a fault, *J. Geophys.*
1185 *Res.*, **98**, 9985–9907, doi:10.1029/93JB00191.
- 1186 Roache, P. (1998), *Verification and Validation in Computational Science and*
1187 *Engineering*, first ed., Hermosa Publishers, Albuquerque.
- 1188 Roten, D., Olsen, K. B., Day, S. M. and Cui, Y. (2016), Quantification of
1189 fault zone plasticity effects with spontaneous rupture simulations, *Work-*
1190 *shop on Best Practices in Physics-Based Fault Rupture Models for Seismic*
1191 *Hazard Assessment of Nuclear Installations*, 18–20 November 2015, Vi-
1192 enna, Unpublished conference paper.
- 1193 Ruina, A. (1983), Slip instability and state variable friction laws, *J. Geophys.*
1194 *Res.*, **88**, B12, 10359–10370, doi:10.1029/JB088iB12p10359.
- 1195 Scalerandi M., Delsanto, P. P., Chiroiu, C. and Chiroiu, V. (1999), Numerical
1196 simulation of pulse propagation in nonlinear 1-D media, *J. Acoust. Soc.*
1197 *Am.*, **106**, doi:10.1121/1.428078.
- 1198 Shi, Z. and Day, S. M. (2013), Rupture dynamics and ground motion from 3-
1199 D rough-fault simulations, *J. Geophys. Res.*, **118**, 1122–1141, doi:10.1002/
1200 jgrb.50094.
- 1201 Shipton, Z. K., Evans, J. P. and Thompson, L. B. (2005), The geometry
1202 and thickness of deformation-band fault core and its influence on sealing
1203 characteristics of deformation-band fault zones, in *Faults, Fluid Flow, and*
1204 *Petroleum Traps*, AAPG Mem., **85**, edited by R. Sorkabi and Y. Tsuji,
1205 181–195, American Association of Petroleum Geologists, Tulsa, Okla.
- 1206 Simo, J. C. and Taylor, R. L. (1985), Consistent tangent operators for rate-
1207 independent elastoplasticity, *Comput. Methods Appl. Mech. Eng.*, **48**, 101–
1208 118, doi:10.1016/0045-7825(85)90070-2.
- 1209 Simo, J. C. and Hughes, T. J. R. (1998), *Computational Inelasticity*, first
1210 ed., Springer, New York, doi:10.1007/b98904.

- 1211 Svärd, M. and Nordström, J. (2014), Review of summation-by-parts schemes
1212 for initial-boundary-value problems, *J. Comput. Phys.*, **268**, 17–38, doi:
1213 10.1016/j.jcp.2014.02.031.
- 1214 Templeton, E. and Rice, J. R. (2008), Off-fault plasticity and earthquake
1215 rupture dynamics: 1. Dry materials or neglect of fluid pressure changes, *J.*
1216 *Geophys. Res.*, **113**, B09306, doi:10.1029/2007JB005529.
- 1217 Thompson, T. B. and Meade, B. J. (2016), Next generation boundary element
1218 models for earthquake science, Poster Presentation at 2016 SCEC Annual
1219 Meeting.
- 1220 Tullis, T. E., Richards-Dinger, K., Barall, M., Dietrich, J. H., Field, E. H.,
1221 Heien, E. M., Kellog, L. H., Pollitz, F. F., Rundle, J. B., Sachs, M. K., Tur-
1222 cotte, D. L., Ward, S. N. and Yikilmaz, M. B. (2012), Generic earthquake
1223 simulator, *Seismol. Res. Lett.*, **83**, 959–963, doi:10.1785/0220120093.
- 1224 Virta, K. and Mattsson, K. (2014), Acoustic wave propagation in complicated
1225 geometries and heterogeneous media, *J. Sci. Comput.*, **61**, doi:10.1007/
1226 s10915-014-9817-1.
- 1227 Xu, S., Ben-Zion, Y. and Ampuero, J.-P. (2012), Properties of inelas-
1228 tic yielding zones generated by in-plane dynamic ruptures: I. Model
1229 description and basic results, *Geophys. J. Int.*, **191**, 1325–1342, doi:
1230 10.1111/j.1365-246X.2012.05679.x.
- 1231 Xu, S., Ben-Zion, Y. and Ampuero, J.-P. (2012), Properties of inelastic yield-
1232 ing zones generated by in-plane dynamic ruptures: II. Detailed parameter-
1233 space study, *Geophys. J. Int.*, **191**, 1343–1360, doi:10.1111/j.1365-246X.
1234 2012.05685.x.